Accepted to Phys. Fluids 10.1063/5.0141156

Effect of nozzle up-scaling on coaxial, gas-assisted atomization

Feichi Zhang,[1] Simon Wachter,[1] Thorsten Zirwes,[2, 3] Tobias Jakobs,[1] Nikolaos Zarzalis,[3] Dimosthenis Trimis,[3]
Thomas Kolb,[1, 4] and Dieter Stapf[1]
[1)]*Institute for Technical Chemistry, Karlsruhe Institute of Technology, 76344, Eggenstein-Leopoldshafen, Germany*
[2)]*Steinbuch Centre for Computing, Karlsruhe Institute of Technology, 76131, Karlsruhe, Germany*
[3)]*Engler-Bunte-Institute: Combustion Technology, Karlsruhe Institute of Technology, 76131, Karlsruhe, Germany*
[4)]*Engler-Bunte-Institute: Fuel Technology, Karlsruhe Institute of Technology, 76131, Karlsruhe, Germany*

(*Electronic mail: feichi.zhang@kit.edu.)

(Dated: 16 February 2023)

Mass flow scaling of gas-assisted coaxial atomizers from laboratory to industrial scale is of major interest for a wide field of applications. However, there is only scarce knowledge and research concerning the effect of atomizer scale-up on liquid breakup and spray characteristics. The main objective of this study is therefore to derive basic principles for liquid jet breakup using up-scaled nozzles to increase the liquid mass flow rate $\dot{M}_{liq}$. For that purpose, atomizers with the same geometrical setup but increased sizes have been designed and experimentally investigated for $\dot{M}_{liq} = 20$, 50, 100, 500 kg/h, while the aerodynamic Weber number We_{aero} and gas-to-liquid ratio GLR have been kept constant. Primary jet breakup was recorded via high-speed imaging and the liquid core length L_C as well as the frequency of the Kelvin-Helmholtz instability f_K were extracted. Applying these results as reference data, highly-resolved numerical simulations have been performed to gain a deeper understanding of the effect of mass flow scaling.

In the case of keeping We_{aero} and GLR constant, it has been shown by both experiments and simulations that the breakup morphology, given by a pulsating liquid jet with disintegration of fiber-type liquid fragments, remains almost unchanged with the degree of up-scaling n. However, the normalized breakup length L_C/d_{liq} has been found to be considerably increased with increasing n. The reason has been shown to be the decreased gas flow velocity v_{gas} at the nozzle exit with n, which leads to a decreased gas-to-liquid momentum flux ratio j and an attenuated momentum exchange between the phases. Accordingly, the calculated turbulence kinetic energy of the gas flow, as well as the specific kinetic energy in the liquid phase decrease with n. This corresponds to a decreased f_{KHI} with n or $\dot{M}_{liq}$, respectively, which has been confirmed by both experiments and simulations. The same behavior has been shown for two liquids with different viscosities and at different We_{aero}. The obtained results allow a first-order estimate of the liquid breakup characteristics, where the influence of nozzle up-scaling can be incorporated into j and Re_{liq} in terms of n.

Keywords: Gas-assisted atomization, mass flow scaling, primary atomization, VOF-LES, OpenFOAM

I. INTRODUCTION

Gas-assisted atomizers with a central liquid jet and coaxial gas stream are commonly utilized in a variety of applications[1] and the underlying physics of breakup phenomena is of fundamental interest to assess the atomization performance. One of the first morphological classifications of the breakup phenomena was derived by Faragò and Chigier for various liquid jet thicknesses[2]. The jet breakup classification was performed using dimensionless numbers such as Re_{liq} and We_{aero}, according to Eq. 1 and Eq. 2. Therewith, liquid jet diameter d_{liq}, velocity v, density ρ, dynamic viscosity η_{liq} and surface tension σ were applied. The gas and liquid phases are represented by the subscripts *gas* and *liq*, respectively.

$$Re_{liq} = \frac{d_{liq} \cdot v_{liq} \cdot \rho_{liq}}{\eta_{liq}} \tag{1}$$

$$We_{aero} = \frac{\left(v_{gas} - v_{liq}\right)^2 \cdot \rho_{gas} \cdot d_{liq}}{\sigma} \tag{2}$$

According to Faragò and Chigier the primary breakup was divided into Rayleigh type, membrane type, and fiber type breakup with increasing We_{aero} between 0 and 100[2]. Whereas the Rayleigh type breakup enables the formation of large droplets, the membrane type breakup leads to gas-filled membranes near the nozzle orifice. The fiber type breakup is characterized by peeled off fibers from the liquid jet while disintegration occurs at the liquid jet core. For a further increase in We_{aero}, two sub-modes, pulsating and superpulsating, subdivide the fiber type breakup in terms of droplet number density fluctuations in the resulting spray[2]. The morphological classification was later expanded by Lasheras and Hopfinger[3], utilizing the momentum flux ratio j (Eq. 3) for the fiber type subdivision.

$$j = \frac{j_{gas}}{j_{liq}} = \frac{v_{gas}^2 \cdot \rho_{gas}}{v_{liq}^2 \cdot \rho_{liq}} \tag{3}$$

As the primary breakup of liquid jets applying coaxial atomizers is shear-driven, the dynamic viscosity of the liquid jet can significantly affect the jet disintegration. The damping effects of increased viscosity on primary jet breakup were investigated by Zhao et al.[4] and Sänger et al.[5,6] The authors found the membrane type breakup to be the most common regime for high-viscosity jets in coaxial atomization. Additionally, for the enhanced membrane formation, pulsating and flapping instabilities were identified that lead to liquid jet displacement in the axial and radial directions. Moreover, it has been shown[7] that the Kelvin-Helmholtz instability caused by aerodynamic forces represents the main mechanism for liquid destabilization, leading to formation of initial waves on the intact liquid surface. Thereafter, the Rayleigh-Taylor instability and aerodynamic interactions result in growth and acceleration of these surface perturbations, until primary liquid fragments protrude and disintegrate from the liquid core.

The work of Dumouchel[8] noted that the discrepancies in geometrical parameters and flow patterns within the nozzles represent the main cause for the inconsistencies of measured breakup morphology in different literature works, which has sparked interest for a more detailed analysis. Investigations on the effect of gas gap width on the primary jet breakup were performed between $d_{gas} = 0.6 - 2$ mm by Wachter et al.[9] In that study, an increase in the gas gap width (which was accompanied by an increase of the gas mass flow) led to a decrease in primary ligament length. This result was explained by an increase in aerodynamic forces and the free jet theory[10]. For an increment in the gas gap width, the exiting gas phase from the nozzle orifice remains at higher velocity over a longer distance, as gas entrainment from the surroundings is reduced[10]. Investigations on the effect of nozzle geometry, especially the liquid jet diameter, were performed by Kumar et al.[11] Here, atomizers with d_{liq} = 4, 6, 8 mm and constant $d_{gas} = 15$ mm were utilized, focusing on the primary breakup with quantitative parameters as an instability frequency and ligament length. For constant $j = 2.8$, while reducing the momentum flow ratio J

$$J = \frac{J_{gas}}{J_{liq}} = \frac{v_{gas}^2 \cdot \rho_{gas} \cdot A_{gas}}{v_{liq}^2 \cdot \rho_{liq} \cdot A_{liq}} \tag{4}$$

an increase in the primary ligament length for higher d_{liq} was detected[11]. The same result has been reported in the experiments[12,13], where a decreased spray angle and a reduced liquid core length were observed at increased J for a two-fluid coaxial atomizer. Leroux et al.[14] performed an experimental investigation of nozzle scale-up and its effects on primary jet breakup, applying three primary jet diameters d_{liq} = 0.4, 1, 2 mm and gas gap widths d_{gas} = 3.5, 6, 8 mm. The comparison of the atomizers was performed for constant Re_{liq} and constant momentum flow ratio J. As a result, the breakup morphology of the performed atomization experiments was not comparable, as low d_{liq} achieved a prompt atomization (or fiber type breakup with superpulsating mode) and high d_{liq} led to long primary ligaments and large droplets[14,15].

In order to gain detailed insights into the breakup behavior of liquid jets, numerical simulations have been extensively applied in recent decades[16–27]. The VOF-LES (Volume of Fluid - Large Eddy Simulation) of a high-viscous liquid shown in Zhang et al.[25,27] revealed that the breakup process is triggered by concentric, axisymmetric ring vortices. Moreover, it has been shown that liquid jets break up faster at elevated pressure and increased gas-to-liquid inclination angle. Direct numerical simulations (DNS) of primary atomization of a round liquid water jet injected into a quiescent environment was presented in[18], indicating that ligament formation is generated via roll-up of the liquid jet tip and disturbances are fed from the liquid jet tip upstream through vortices. The DNS performed by Zandian et al.[19] distinguished three atomization cascades for the primary atomization of a planar liquid jet based on Re_{liq} and We_{aero}. The breakup process of a planar prefilming airblast atomizer has been studied using DNS[26], which exhibited reasonably good agreement with the experimental results. Although the resolution is limited by the cell size used in the numerical simulations, large-scale structures of the liquid phase, including destabilization of the intact jet core, as well as the primary ligaments disintegrated from the jet core, can be properly resolved. This is attributed to the fact that the breakup process of the liquid jet is dominated by large-scale, coherent vortices in the gaseous phase close to the liquid core, that can be resolved by relatively coarse grids[25].

Taking a closer look at the literature reveals that previous studies mostly have applied gas-assisted atomizers at laboratory scale along with relatively low liquid mass flow rates. Relevant studies combining the effects of single parameters on the resulting primary breakup, as is necessary for the liquid mass flow scale-up of coaxial atomizers, are scarce. Therefore, the objective of this work is to assess the effect of using up-scaled nozzles concerning mass flow scaling on the breakup performance of liquid jets. In a previous study[28], the authors performed experimental investigations on the scale-up of coaxial gas-assisted atomizers from laboratory-scale mass flows towards industrial scale mass flows. For that purpose, a scaling approach based on constant aerodynamic Weber number We_{aero} and gas-to-liquid ratio GLR was employed and an empirical model for the generated droplet diameters within the spray located far downstream of the nozzle was derived. The current work represents a follow-on study of the work by Wachter et al.[28], which incorporates time-resolved numerical simulations for a more detailed understanding of the breakup morphology of the liquid jet while up-scaling the nozzle or $\dot{M}_{liq}$. The resolved flow dynamics, i.e., flow velocities and kinetic energies, provide an insight into the three-dimensional, multiphase interactions close to the liquid jet, which allows to reveal the physical mechanisms behind the phenomenological behavior of liquid jets observed in experiments. The experiments are used to guide the simulations with respect to their validity with respect to the observed correlations of breakup morphology with the degree of up-scaling. Moreover, additional credibility is given by the experiments considering large nozzle or $\dot{M}_{liq}$, which is beyond the computational limit.

II. EXPERIMENTAL CONDITIONS

The gas-assisted coaxial atomizer used in this work is shown in Fig. 1, which has been investigated extensively in the last years concerning the influences of nozzle design and operating parameters on the breakup of liquid jets [5,6,9,23,25,27–31]. The diameters of the liquid nozzle and annular gas nozzle are

Accepted to Phys. Fluids 10.1063/5.0141156

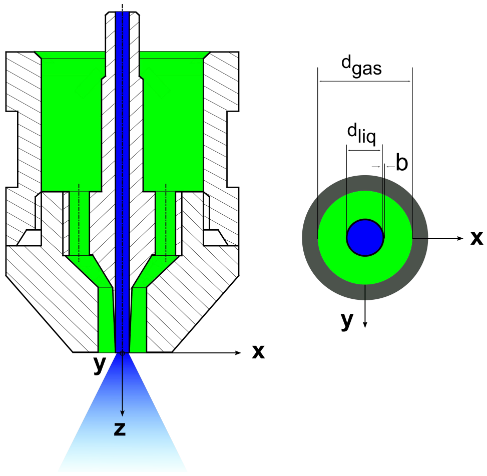

FIG. 1. Schematic view of the applied gas-assisted coaxial atomizer with central liquid jet (blue) and annular gas stream (green).

given by d_{liq} and d_{gas}. The thickness of the nozzle wall for the liquid jet is b. The setup of the nozzle remains the same while the outlet area of the nozzle increases proportionally with the liquid mass flow rate $\dot{M}_{liq}$. The atomizer dimensions corresponding to the respective $\dot{M}_{liq}$ are given in Tab. I. As the aerodynamic Weber number We_{aero} and gas-to-liquid ratio GLR represent the most relevant parameters applied for process scaling, an approach that keeps We_{aero} and GLR constant was selected for mass flow scale-up for the investigated nozzles. In this way, the liquid flow velocity v_{liq} was kept constant with increased $\dot{M}_{liq}$ or d_{liq}, respectively.

TABLE I. Nozzle orifice dimensions of the scaled atomizers

$\dot{M}_{liq}$ in kg/h	d_{liq} in mm	b in mm	d_{gas} in mm
20	2.0	0.1	5.3
50	3.2	0.1	9.2
100	4.5	0.1	14.1
500	10.0	0.1	37.3

The experiments have been conducted under atmospheric condition, applying water and a glycerol/water mixture with different physical properties. The dynamic viscosity, surface tension and density of the liquids are η_{liq} = 1 mPa·s, σ_{liq} = 0.0719 N/m and $\rho_{liq} = 998$ kg/m^3 for water, and $\eta_{liq} = 100$ mPa·s, $\sigma_{liq} = 0.0649$ N/m and $\rho_{liq} = 1220$ kg/m^3 for the glycerol/water mixture. Air was used as atomizing gas with a viscosity of $\mu_G = 0.0185$ and a density of $\rho_G = 1.182$ kg/m^3. The operating conditions for different nozzle sizes or $\dot{M}_{liq}$ are given in Tab. II.

TABLE II. Operating conditions used in the experiments.

		1 mPa·s				100 mPa·s			
$\dot{M}_{liq}$	We_{aero}	v_{gas}	GLR	j	J	v_{gas}	GLR	j	J
kg/h	-	m/s	-	-	-	m/s	-	-	-
20	250	88	0.36	2.99	17.90	83	0.33	3.25	18.89
50	250	70	0.36	1.89	14.24	66	0.33	2.05	15.02
100	250	59	0.36	1.35	12.00	56	0.33	1.48	12.74
500	250	40	0.36	0.62	8.14	-	-	-	-
20	500	124	0.50	5.95	35.03	117	0.47	6.45	37.92
50	500	98	0.50	3.71	27.68	93	0.47	4.08	30.14
100	500	83	0.50	2.66	23.45	79	0.47	2.94	25.61
500	500	56	0.50	1.21	15.82	-	-	-	-
20	750	151	0.61	8.82	52.04	143	0.57	9.64	56.21
50	750	120	0.61	5.57	41.36	114	0.57	6.13	44.81
100	750	101	0.61	3.94	34.81	96	0.57	4.34	37.74
500	750	68	0.61	1.79	23.44	-	-	-	-
20	1000	174	0.70	11.71	68.81	165	0.66	12.83	75.10
50	1000	138	0.70	7.36	54.58	131	0.66	8.09	59.63
100	1000	117	0.70	5.29	46.27	111	0.66	5.81	50.52
500	1000	79	0.70	2.41	31.24	-	-	-	-

As the experimental conditions cover a large range of $\dot{M}_{liq}$ up to 500 kg/h, two different spray test rigs were utilized. The spray test rig (ATMO), which is described in detail in Wachter et al.[32], was applied for liquid mass flows at the lab-scale between $\dot{M}_{liq} = 20 - 100$ kg/h. The burner test rig (BTR), which is described in further detail elsewhere[28], was employed for the investigations of the nozzles featuring $\dot{M}_{liq}$ up to an industrial scale of 500 kg/h. As the BTR test facility was not equipped with a suction system, experiments with glycerol/water mixtures were not applicable for $\dot{M}_{liq} = 500$ kg/h. More details of the nozzle system considering mass flow up-scaling can be found in Wachter et al.[28]

Although the most important operating parameters, i.e., GLR and We_{aero}, are kept constant, other characteristic parameters such as J and j are inevitably changed while up-scaling the nozzle due to a decrease in v_{gas} according to the chosen scaling approach (see Tab. II). In the following sections, the scaling factor n representing the ratio of the value used and the reference (smallest considered) liquid mass flow rate $\dot{M}_{liq,0} = 20$ kg/h

$$n = \frac{\dot{M}_{liq}}{\dot{M}_{liq,0}} \tag{5}$$

is introduced to discuss its influence on the atomization behavior. As the velocity of liquid flow v_{liq} remains constant, the outlet area of the liquid stream A_{liq} increases proportionally with n ($A_{liq} \propto n^1$), leading to an increased d_{liq} with n by $d_{liq} \propto n^{1/2}$ (see Eq. 6). Due to $We_{aero} = const.$, the nozzle exit velocity of the gas v_{gas} decreases with n by $v_{gas} \propto n^{-1/4}$ (see Eq. 7). Furthermore, the constant GLR results in a linear increase of $\dot{M}_{gas}$ with n, so that the outlet area of the gas flow

Accepted to Phys. Fluids 10.1063/5.0141156

scales with n by $A_{gas} \propto n^{5/4}$ (see Eq. 8). The modifications of these basic parameters with n while applying the provisions of constant v_{liq}, We_{aero} and GLR are summarized in Eq. 6-8

$$\begin{aligned} & v_{liq} = const. \\ \Rightarrow & A_{liq} = \frac{\dot{M}_{liq}}{\rho_{liq} \cdot v_{liq}} = \frac{n \cdot \dot{M}_{liq,0}}{\rho_{liq} \cdot v_{liq}} \propto n^1 \\ \Rightarrow & d_{liq} \propto A_{liq}^{1/2} \propto n^{1/2} \end{aligned} \tag{6}$$

$$\begin{aligned} We_{aero} &= \frac{\left(v_{gas} - v_{liq}\right)^2 \cdot \rho_{gas} \cdot d_{liq}}{\sigma} = const. \\ \Rightarrow v_{gas} &\propto n^{-1/4} \quad \text{with} \quad v_{gas} \gg v_{liq} \end{aligned} \tag{7}$$

$$\begin{aligned} & GLR = const. \Rightarrow \dot{M}_{gas} \propto n^1 \\ \Rightarrow & A_{gas} \propto \frac{\dot{M}_{gas}}{v_{gas}} \propto n^{5/4} \end{aligned} \tag{8}$$

which lead to the following correlations of the characteristic dimensionless parameters j, J and Re_{liq} with n

$$j = \frac{v_{gas}^2 \cdot \rho_{gas}}{v_{liq}^2 \cdot \rho_{liq}} \propto n^{-1/2} \tag{9}$$

$$J = \frac{v_{gas}^2 \cdot \rho_{gas} \cdot A_{gas}}{v_{liq}^2 \cdot \rho_{liq} \cdot A_{liq}} \propto n^{-1/4} \tag{10}$$

$$Re_{liq} = \frac{d_{liq} \cdot v_{liq} \cdot \rho_{liq}}{\eta_{liq}} \propto n^{1/2} \tag{11}$$

Eq. 9-11 reveal a decrease of j, J and an increase of Re_{liq} with n at constant v_{liq}, We_{aero} and GLR. Accordingly, an increase of the liquid jet core length L_C with n is expected based on the correlations derived from previous experiments of coaxial liquid jets for L_C as functions of We_{aero} and j[8].

For detection of the primary jet breakup, a high-speed camera was used with an appropriate light-emitting diode (LED) array in backlight configuration, featuring an illumination of 9 × 4500 lm. For every operating condition, 2000 images were taken at the nozzle orifice. The camera allowed for images with 1 megapixel at a 3600 Hz frame rate. A more detailed description of the setup is given in our previous work[31]. Detection of the primary ligament length was performed in post-processing by applying the threshold method of Otsu et al.[33] for the glycerol-water experiments with the lowest Weber number. In order to determine the average primary ligament length and eliminate the influence of double detection, every tenth high-speed camera image was analyzed.

The KHI (Kelvin-Helmholtz instability) wave peak was measured at $z = 2 \cdot d_{liq}$ downstream of the nozzle orifice via line method and analyzed with a Fast Fourier Transformation (FFT) according to Sänger and Kapur[6,34]. All measurements were evaluated also in accordance with the Nyquist criterion for frequency analysis[35]. The results were compared with atomization instability theory according to Marmottant and Villermaux[7], which defines the KHI frequency f_{KHI} as a function of shear layer thickness δ_{gas} and Dimotakis vertical wave velocity v_{KHI} (see Eq. 12-14)[36,37].

$$f_{KHI} \propto \frac{v_{KHI}}{\delta_{gas}} \cdot \left(\frac{\rho_{gas}}{\rho_{liq}}\right)^{1/2} \tag{12}$$

$$\delta_{gas} \propto s_{gas} \cdot Re_{gas}^{-1/2} \tag{13}$$

$$v_{KHI} = \frac{\sqrt{\rho_{liq}} \cdot v_{liq}}{\sqrt{\rho_{liq}} + \sqrt{\rho_{gas}}} + \frac{\sqrt{\rho_{gas}} \cdot v_{gas}}{\sqrt{\rho_{liq}} + \sqrt{\rho_{gas}}} \tag{14}$$

III. SIMULATION OF MULTIPHASE FLOW

The nozzle setup proposed in section II has been numerically simulated in this work to reveal details of the multiphase interactions during the nozzle scale-up. Due to the use of relatively large $\dot{M}_{liq}$ and nozzle size, the simulations have been conducted solely for the glycerol/water mixture with $\dot{M}_{liq}$ = 20, 50, 100 kg/h. The GLR and We_{aero} were set to $GLR = 0.36$ and $We_{aero} = 250$. In this way, the numerical simulations reproduce the multiphase flow field in the vicinity of the liquid jet with a reasonably good resolution, which allows a thorough understanding of the physical mechanism responsible for the observed behavior of liquid jet breakup due to nozzle up-scaling. In contrast, the experiments have been conducted additionally for water jets, employing a wider range with $250 \leq We_{aero} \leq 1000$ and $\dot{M}_{liq}$ up to 500 kg/h, which extends the general validity of the obtained results.

A. Mathematical formulations

Considering the multiphase interaction, the volume of fluid (VOF) method has been used to simulate the multiphase flow, which captures the liquid-gas interface by means of the liquid volume fraction f. An additional equation for the liquid volume fraction f is solved for the VOF method

$$\partial_t f + \nabla \cdot (\tilde{\mathbf{u}} f) + \nabla \cdot (f(1-f)\tilde{\mathbf{u}}_r) = 0 \tag{15}$$

f represents the volume fraction of the liquid phase, creating a virtual single-phase fluid. The relative velocity $\tilde{\mathbf{u}}_r$ between the liquid and gas phases in Eq. 15, also called the compression velocity, is calculated from

$$\mathbf{u}_r = \mathbf{u}_{liq} - \mathbf{u}_{gas} = |\mathbf{u}|\ \mathbf{n} = |\mathbf{u}|\ \frac{\nabla f}{|\nabla f|} \tag{16}$$

where $\mathbf{n}$ is the surface normal unit vector[38]. In this manner, $f = 1$ indicates the pure liquid phase and $f = 0$ the pure gas phase. Consequently, the intermediate values of $0 < f < 1$ identify the gas-liquid interface. The evolution equation for f has been derived from mass balance equations for both phases, which results in the mentioned extra term. The numerical effect is a compression of the interface, to keep a physical sharp transition of f between 0 and 1, which thus counteracts numerical diffusion of the interface over time. The term is active

Accepted to Phys. Fluids 10.1063/5.0141156

only within the interface zone with $0 < f < 1$ and vanishes at both limits of phase fractions. A detailed description and derivation for Eq. 15 as well as its implementation in OpenFOAM can be found elsewhere[39].

The turbulent flow is described in terms of the large eddy simulation (LES) technique[40]. The LES approach is based on filtering the flow field spatially, which resolves large turbulent vortices and models the effects of unresolved eddies by means of the sub-grid scale (sgs) model. Whereas the large eddies generally depend on the geometry of the bounded flow domain and show a non-isotropic behavior, the small eddies exhibit more universal, isotropic features. Therefore, resolving directly large-scale flow structures and modelling those fine turbulent vortices in analogy to the Reynolds-Averaged Navier-Stokes (RANS) approach with an eddy viscosity model is well suited for studying the near-field flow dynamics during primary breakup of co-axial liquid jets. The cut-off scale in this case represents the filter length, which is related to the grid resolution since LES with implicit filtering is conducted. Below the cut-off scale, flow structures with sizes smaller than it cannot be resolved. In the framework of LES, the compressible Navier-Stokes equations solved in this work are given by

$$\partial_t \bar{\rho} + \nabla\cdot(\bar{\rho}\tilde{\mathbf{u}}) = 0 \tag{17}$$

$$\begin{aligned}\partial_t(\bar{\rho}\tilde{\mathbf{u}}) + \nabla\cdot(\bar{\rho}\tilde{\mathbf{u}}\tilde{\mathbf{u}}) = -\nabla\bar{p} + \nabla\cdot(\bar{\tau}+\bar{\tau}^{sgs}) \\ +\bar{\rho}\mathbf{g} + \bar{\mathbf{F}}_\sigma\end{aligned} \tag{18}$$

$$\partial_t(\bar{\rho}\tilde{e}) + \nabla\cdot(\rho\tilde{\mathbf{u}}\tilde{e}) = -\nabla\cdot(\bar{p}\tilde{\mathbf{u}}) - \nabla\cdot\left(\bar{\mathbf{j}}_q + \bar{\mathbf{j}}_q^{sgs}\right) \tag{19}$$

where $\bar{\cdot}$ denotes spatially filtered and $\tilde{\cdot}$ Favre-filtered values of a compressible flow. ρ is the gas density, $\mathbf{u}$ the velocity vector, p the pressure, and $\mathbf{g}$ the gravitational acceleration. $e = \int_0^T c_v \mathrm{d}T + 0.5|\mathbf{u}|^2$ denotes the specific total internal energy with the isochoric heat capacity c_v and the temperature T. The shear stress tensor is evaluated based on the gradient of the velocity field $\tau = \eta(\nabla\mathbf{u} + \nabla\mathbf{u}^T - \frac{2}{3}\nabla\cdot\mathbf{u}\, I)$ with the unit tensor I. $\bar{\mathbf{j}}_q = -\lambda\nabla T$ is the heat flux due to thermal conduction, with λ being the thermal conductivity. The sgs stress tensor $\bar{\tau}^{sgs}$ in Eq. 19 is evaluated by means of sgs turbulence modeling[40]

$$\bar{\tau}^{sgs} = \bar{\rho}(\tilde{\mathbf{u}}\tilde{\mathbf{u}} - \widetilde{\mathbf{u}\mathbf{u}}) = -2\bar{\rho}\nu_{sgs}\tilde{S}_{ij} \tag{20}$$

with the turbulent or sgs viscosity ν_{sgs} and the filtered strain rate tensor $\tilde{S}_{ij}$. The sgs heat flux $\bar{\mathbf{j}}_q^{sgs}$ in Eq. 19 is calculated via a gradient transport approach in a similar way by

$$\bar{\mathbf{j}}_q^{sgs} = \bar{\rho}(\tilde{\mathbf{u}}\tilde{e} - \widetilde{\mathbf{u}e}) = -\bar{\rho}\frac{\nu_{sgs}}{Pr_t}\nabla\tilde{e} \tag{21}$$

The wall-adapted local eddy viscosity (WALE) model has been applied in this study to evaluate ν_{sgs} and the turbulent Prandtl number Pr_t is set to unity.

In the current implementation of the VOF method in OpenFOAM, the surface tension at the liquid-gas interface generates an additional pressure gradient resulting in a net force $\bar{\mathbf{F}}_\sigma = \sigma\kappa\nabla f$, where κ is the curvature of the interface. Following the continuum surface force (CSF) model by Brackbill et al.[41], this force is evaluated per unit volume in the current work and the curvature of the gas-liquid interface is computed from divergence of the surface unit normal vector. Albadawi et al.[42] proposed a coupled VOF with the Level Set method for improved surface tension calculation, which has shown better results than the original VOF method in OpenFOAM when the influence of surface tension dominates. Similar conclusions have been drawn[43] for a model concerning sub-grid scale surface tension for LES, which is best suited for surface tension-dominated flows. In this work, the aerodynamic force dominates the surface tension force due to $We_{aero} \gg 1$ and therefore the effect of surface tension modelling is subordinate. The material properties of the liquid-gas mixture, i.e., the density and viscosity, are calculated based on the volume-weighted average in terms of f.

$$\begin{aligned}\rho &= f\cdot\rho_{liq} + (1-f)\cdot\rho_{gas} \\ \eta &= f\cdot\eta_{liq} + (1-f)\cdot\eta_{gas}\end{aligned} \tag{22}$$

B. Computational setup

The computational domains used for the simulation were constructed according to the experimental design of the nozzle, which is depicted in Fig. 2. It covers a major part of the nozzle geometry in order to resolve the internal flow within the nozzle. The liquid and air inlets start from a length of $8.6d_{liq}$ upstream the nozzle exit plane. The nozzle section is connected to a cone-shaped domain downstream, which has a length of $30d_{liq}$ and diameters of $10d_{liq}$ and $20d_{liq}$ at the nozzle exit and outlet. The domain length and width have been selected based on a compromise in terms of simulation accuracy and available computational resources, which allows the use of refined grid resolution in the near-nozzle zone and zero-gradient type boundary conditions at the open boundaries. Note that the web thickness b (see Fig. 1 and Tab. I) connecting the central liquid nozzle and annular air nozzle is kept constant during up-scaling the nozzle, therefore, the geometries used for different n are not scalable to each other. The x-axis indicates the streamwise direction and the origin of the coordinate system, which is located at the center of the nozzle exit.

The computational grids for differently scaled nozzles consist of approximately 10.3 million hexahedral elements, which are locally refined close to the primary atomization zone that encloses the intact liquid jet. The mesh topology as well as the total number of grid cells remain constant while up-scaling the nozzle, so that the grid resolution reduces while up-scaling the nozzle or mass flow rate. The smallest resolutions for $\dot{M}_{liq}$ = 20, 50, 100 kg/h were $\Delta_{min,r}$ = 25, 32, 50 μm in the radial direction and $\Delta_{min,x}$ = 50, 64, 100 μm in the streamwise direction. The grid size expands outwardly with a small rate in the radial and streamwise directions. The grid resolution is not fine enough to resolve small-scale liquid ligaments or droplets for the given conditions with high We_{aero} and Re_{gas}. However, particular focus of this work is to study the primary breakup behavior of the intact liquid core, which can be resolved on the current grid. The grid resolution used for the smallest nozzle with $d_{liq} = 2$ mm is sufficient for resolving the breakup process of the liquid jet according to our previous studies, which shows grid-independence for the calculated

Accepted to Phys. Fluids 10.1063/5.0141156

breakup length with further refined mesh[25]. For the larger or up-scaled nozzles, however, the primary breakup process can be under-resolved. To conform this behavior, an additional simulation has been performed for the largest nozzle at 100 kg/h using a twice-refined grid (with over 81 million cells). The refined simulation has been deliberately made to reveal the impact of grid resolution and to point out the difficulties arising in highly resolved simulations for large-scale atomization systems.

The boundaries of the computational domain are indicated in Fig. 2. There, the no-slip condition was used for the nozzle walls, whereas mass flow rates corresponding to the experiments were given for the gas and liquid inlets. The temperature was prescribed at 293 K at all inlets. The volume fraction of the liquid phase f was set to zero at the gas inlet and unity at the liquid inlet. The specific boundary condition in OpenFOAM called “fixedFluxPressure” has been used for the pressure at the inlet, which adjusts the pressure gradient such that the mass flux corresponds to the one specified by the velocity boundary condition. In this case, two different interpolation schemes are utilized to determine the pressure gradient: First, the mass flux is interpolated to the boundary faces as part of the general pressure correction step of the PIMPLE algorithm following the Rhie-Chow approach. Secondly, the mass flux computed from the current density and velocity fields based on the cell centers is linearly interpolated to the boundary faces. The difference between these two mass fluxes serves as predictor to compute new pressure gradients. This is done iteratively until a pressure gradient is found where both interpolations yield the desired inflow mass flux. At the outlet and entrainment boundaries (see Fig. 2), gradients of flow velocities and f are set to zero if the flow is directed out of the domain and to a fixed value based on the patch normal fluxes if the flow is directed into the domain. The total pressure, in subsonic formulation, is set to 1 bar. Since these far field boundaries are sufficiently far away from the jet core, they are not expected to affect the numerical results regarding breakup morphology.

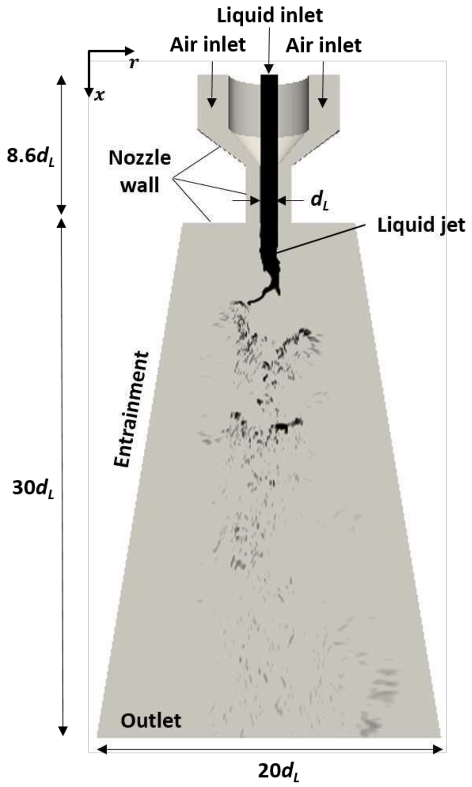

FIG. 2. Computational domain and boundary conditions used for simulations of primary breakup of a co-axial liquid jet.

The balance equations 15-19 were solved numerically using the finite volume method in the framework of the open-source CFD program OpenFOAM[44]. An implicit scheme of second order accuracy (Crank Nicolson) for time integration is used. The Van Leer 2nd order total variation diminishing (TVD) scheme and the unbounded 2nd order upwind scheme have been used for discretizations of the convection terms in the balance equation of f and in the momentum equation. The time step was set to Δt = 0.125, 0.25 and 0.5 μs, allowing a maximum CFL (Courant-Friedrichs-Lewy) number below 0.6. Statistical averaging of the flow has been performed for approximately 500,000 time steps, which corresponds to more than 10 flow-through times based on the bulk velocity of the liquid.

IV. RESULTS

The results of the investigation on primary breakup of liquid jets are subdivided into two sections. The first section contains the experimental results of the high-speed camera images for both investigated liquids, whereas in the second part the results of the numerical simulations are shown.

A. Experimental results

Figure 3 presents the high-speed camera images of the jet breakup under various operating conditions ($\dot{M}_{liq}$ = 20, 50, 100, 500 kg/h and We_{aero} = 250, 500, 750, 1000) using water. All operating conditions in We_{aero} and $\dot{M}_{liq}$ led to the fiber type regime breakup. Especially for high We_{aero} and low $\dot{M}_{liq}$, the superpulsating sub-mode could be detected, characterized by droplet number density fluctuations in the resulting spray. Due to the intensive interaction between gas and liquid phase in combination with low viscosity, the characteristic KHI wave was not detectable in this case.

Accepted to Phys. Fluids 10.1063/5.0141156

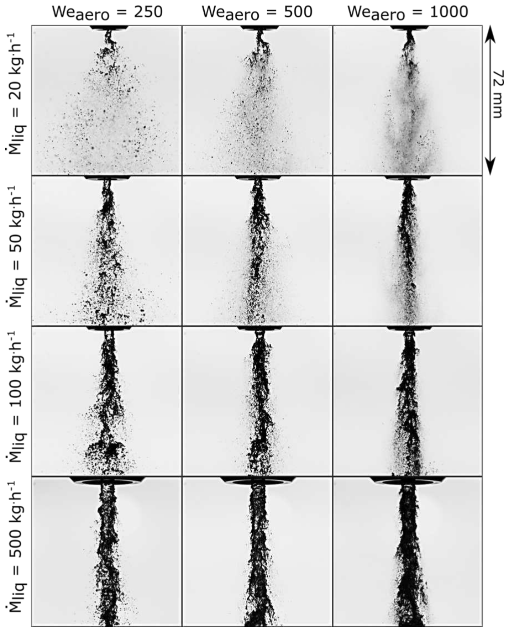
We$_{aero}$ = 250
We$_{aero}$ = 500
We$_{aero}$ = 1000
72 mm
Ṁ$_{liq}$ = 20 kg·h^{-1}
Ṁ$_{liq}$ = 50 kg·h^{-1}
Ṁ$_{liq}$ = 100 kg·h^{-1}
Ṁ$_{liq}$ = 500 kg·h^{-1}

FIG. 3. Snapshots of the primary jet breakup of the water jet at $\dot{M}_{liq}$ = 20, 50, 100, 500 kg/h and We_{aero} = 250, 500, 1000.

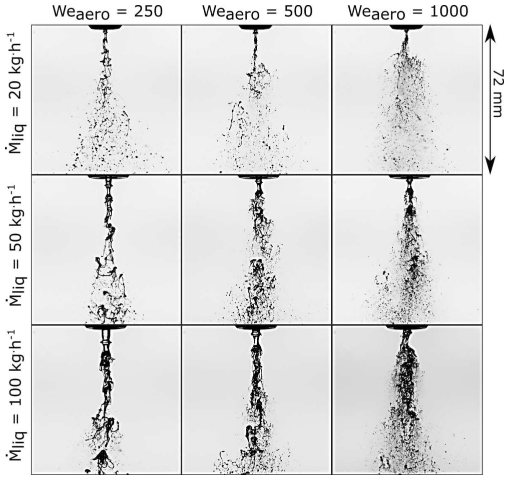
We$_{aero}$ = 250
We$_{aero}$ = 500
We$_{aero}$ = 1000
72 mm
Ṁ$_{liq}$ = 20 kg·h^{-1}
Ṁ$_{liq}$ = 50 kg·h^{-1}
Ṁ$_{liq}$ = 100 kg·h^{-1}

FIG. 4. Snapshots of the primary jet breakup applying the glycerol/water mixture at $\dot{M}_{liq}$ = 20, 50, 100 kg/h and We_{aero} = 250, 500, 1000.

For an increase in We_{aero} a decrease in the droplet size and primary breakup length is observed. This effect can be explained by an increase in aerodynamic forces and higher relative velocities between the exiting gas and liquid phase[28]. The scale-up of the nozzles towards increased $\dot{M}_{liq}$ led to a significant increase in primary ligament length. As shown in Fig. 3, particularly for low We_{aero} at high $\dot{M}_{liq}$, the shear forces of the exiting gas phase are insufficient for disintegrating the liquid jet core, which remains undisturbed over a long distance. Nonetheless, for $We_{aero} = 1000$ and $\dot{M}_{liq}$ = 500 kg/h, the sheared off fibers are subsequently disintegrated into fine droplets, while the liquid jet core remains intact. The increment of primary ligament length L_C can be attributed to a decrease in j and J, as the gas velocity decreases with $\dot{M}_{liq}$, as shown in Eq. 9-10. Therefore, using constant We_{aero} and GLR is not sufficient to achieve the same atomization quality for up-scaled nozzle size or mass flow rate.

Figure 4 depicts the high-speed camera images of primary jet breakup for the glycerol/water mixture with η_{liq} = 100 mPa·s. The influences of We_{aero} and $\dot{M}_{liq}$ on the breakup behavior remain similar for both low- and high-viscous fluids, where an increase of L_C with increasing $\dot{M}_{liq}$ and decreasing We_{aero} can be detected. However, the droplet number density in the spray is significantly reduced and ligament formation is enhanced especially at low We_{aero} for the high-viscous liquid, which is attributed to the increased viscous force with η_{liq}. The measured L_C for the glycerol/water mixture at different mass flow rates is illustrated in Fig. 7 in the next section along with the simulation results, where L_C increases with the degree of mass flow scaling at constant We_{aero}.

B. Simulation results

1. *Breakup morphology*

In Fig. 5, instantaneous iso-surfaces of the liquid volume fraction $f = 0.5$ are used to visualize the liquid jet for different nozzle scales. In accordance with the experimental results from high-speed imaging shown in Fig. 4, the simulations reveal a pulsating-type breakup of the intact jet core along with disintegration of membrane- and fiber-shaped ligaments for all scaled nozzles. The breakup mechanism remains unchanged with increased nozzle sizes. However, the thickness and length of the primary liquid jet increase with up-scaled mass flow rate or nozzle size.

Figure 6 depicts profiles of the time-mean and root mean square (rms) values of f along the centerline axis. The breakup of the liquid jet results in a steep decrease of $\bar{f}$ from 1 (intact liquid core) to 0 (air) along the axis, which leads to spatial discontinuities and temporal fluctuations of f. According to $0 \leq f \leq 1$, the maximum value of f_{rms} is 0.5, which occurs under the conditions of $\bar{f} = 0.5$ and assumes a bimodal distribution of f with equally weighted probabilities for $f = 0$ and $f = 1$. Consequently, the position of $f_{rms,max} \approx 0.5$ is almost co-located with that of $\bar{f} \approx 0.5$ (see the intersection points between profiles of $\bar{f}$ and f_{rms} in Fig. 6), which is used to identify the liquid core length L_C from the simulations.

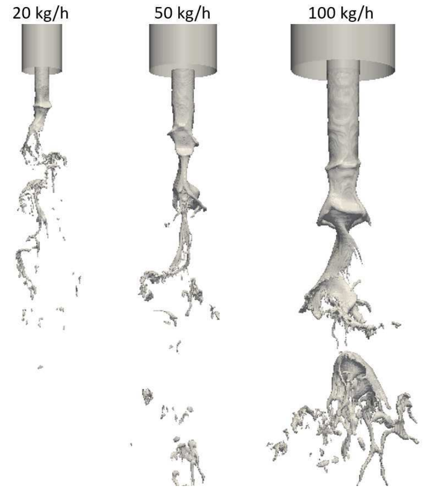

FIG. 5. Iso-surfaces of calculated liquid volume fraction at $f = 0.5$ for up-scaled nozzles.

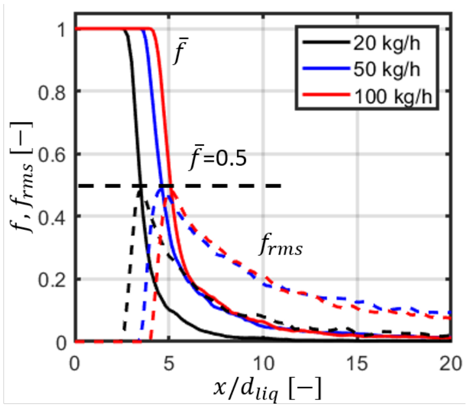

FIG. 6. Streamwise profiles of calculated time-mean and root mean squared values of liquid volume fraction $\bar{f}$ and f_{rms} from VOF-LES of up-scaled mass flows.

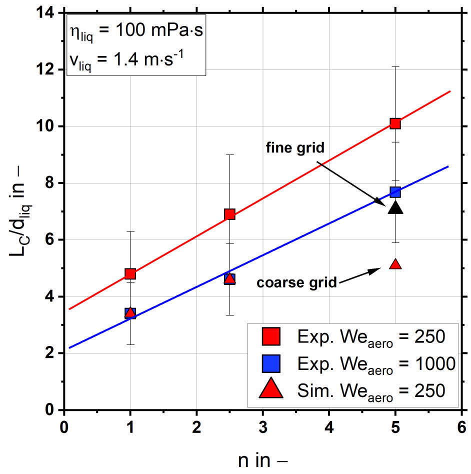

FIG. 7. Comparison of calculated and measured dimensionless primary ligament length at $\dot{M}_{liq}$ = 20, 50, 100 kg/h for the glycerol/water mixture with η_{liq} = 100 mPa·s.

In this way, the calculated L_C (triangle symbols) normalized by the corresponding nozzle diameter is shown in Fig. 7 together with L_C obtained from experiments (square symbols). L_C/d_{liq} increases with n, which has been confirmed in both experiments and simulations. The solid lines in Fig. 7 indicate fitted lines for the experimental results of L_C/d_{liq} vs. n by means of a linear function $L_C/d_{liq} = a \cdot n + b$, with the fitting coefficients a and b. In this way, the scaling rate a is calculated to $a = 1.3$ for $We_{aero} = 250$ (red squares) and $a = 1.1$ for $We_{aero} = 1000$. Note that L_C derived from the experiment is based on line-of-sight imaging shown in Fig. 4, whereas L_C is determined from profiles of calculated liquid volume fraction along the centerline axis in the simulations (see Fig. 6). The deviations between the measured and calculated L_C are therefore caused by the different evaluation methods. As liquid fragments stripping-off from the jet core obscure the observation of the breakup location along the centerline axis, the measurement records an extended L_C based on disintegrated primary ligaments. From the point of view of the numerical simulation, the liquid fragments disintegrated from the jet core cannot be resolved sufficiently due to the limitation given by the grid resolution. Consequently, the same evaluation method for L_C cannot be applied for both experiment and simulation.

We_{aero} measures the ratio of aerodynamic or drag force caused by the velocity difference between the phases and the cohesive forces due to surface tension. With increased gas flow velocity or We_{aero}, the liquid surface is stretched more strongly by the gas flow, which leads to a more intense breakup of the liquid jet. Therefore, L_C at $We_{aero} = 1000$ is smaller compared with L_C at $We_{aero} = 250$ for the measured data, as shown in Fig. 7.

As mentioned in Sec. III B, the total number of grid cells is kept constant (about 10 million) while up-scaling the nozzle, so that the spatial grid resolution decreases for up-scaled nozzles. In order to reveal the impact of grid resolution and to emphasize the difficulties while applying highly resolved simulations for large-scale atomization systems, a twice-refined grid applying a minimum resolution of $\Delta_{r,min} = 25\ \mu$m and 81 million cells has been conducted for the 100 kg/h case using the largest nozzle. As shown in Fig. 7, using the fine grid for the

Accepted to Phys. Fluids 10.1063/5.0141156

100 kg/h nozzle results in a significant increase of L_C (indicated by black triangle) compared with that obtained using the reference grid (indicated by “coarse grid”). Therefore, a grid-independence of L_C is not given for this case. According to our previous study[25], changing $\Delta_{r,min}$ from 25 μm (currently used for the smallest nozzle) to 12.5 μm has led to almost the same L_C compared with the result derived from the reference mesh, indicating that a grid-independence for L_C can be achieved by using $\Delta_{r,min} = 25$ μm. This resolution however would be computationally too expensive for the largest nozzle. Note that the required computing time increases by a factor of 16 by using a twice-refined grid due to 8 times increased cell number and reduced simulation time step by half.

In fact, both VOF and LES methods are essentially limited by grid resolution by definition, which resolve the multiphase flow down to the cut-off scale given by the grid length. The current grid resolution is unable to resolve the droplets within the spray further downstream. However, dominant near-field flow patterns prevailing the multiphase interactions, which cause destabilization of the intact liquid core and disintegration of primary liquid fragments, can be captured.

In the following, the causes leading to the morphological features shown in this section will be elucidated with the help of detailed analysis of the resolved turbulent flow fields and dynamic behavior of the liquid jet.

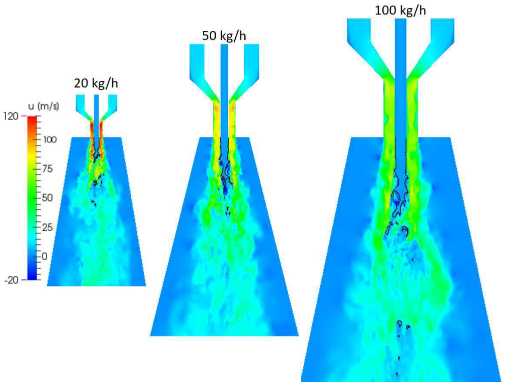

FIG. 8. Instantaneous contours of streamwise velocity u and iso-contours of $f = 0.5$ for up-scaled mass flow rate.

2. *Turbulent flow fields*

The breakup of the liquid jet is triggered by aerodynamic forces exerted by the high-speed gas flow on the low-speed liquid jet, which lead to stretching of liquid surface and an increase of the kinetic energy in the liquid phase. Therefore, the flow patterns of the gas close to the liquid jet plays a decisive role for the breakup process. The atomization process is enhanced by turbulent fluctuations in the gas flow through multiphase momentum exchange, which are further elucidated in Fig. 8 by means of instantaneous contours of the streamwise velocity u on a meridian cutting-plane. The liquid jet surface is indicated in Fig. 8 by the iso-contours of $f = 0.5$. The annular gas flow is accelerated when passing through the convergent section within the nozzle, which reaches a maximum flow velocity at the nozzle exit with $u_{max} \approx 100$ m/s. In contrast, the central liquid stream yields a velocity of approximately 1.4 m/s. The large velocity gradients between the central liquid and surrounding gas flows result in a strong momentum transfer from the gas to the liquid phase, where aerodynamic forces exerted by the gas flow on the liquid surface overwhelm the cohesive surface tension force of the liquid phase, leading to breakup of the liquid jet.

A zoomed view of the turbulent flow field close to the nozzle exit is depicted in Fig. 9 for the case with 20 kg/h, which illustrates the breakup mechanism due to the gas-liquid interaction. The liquid jet in Fig. 9 is indicated by the iso-contour of $f = 0.5$ and the arrows denote flow directions of the gas flow. The liquid jet is stretched and deformed by the high-speed airflow in an initial stage, which results in formation of surface waves on the liquid column. Further downstream, large concentric ring vortices with a length scale of the order of the nozzle diameter are generated, which penetrate into the liquid jet core at its tip and hinder its growth. The strong recirculation of the gas flow can be identified by the blue region near the tip of liquid jet. Afterwards, the protruding tip of the liquid jet is elongated by the airflow until first liquid ligaments pinch off from the jet. Further downstream, these primary ligaments break into thin liquid fibers.

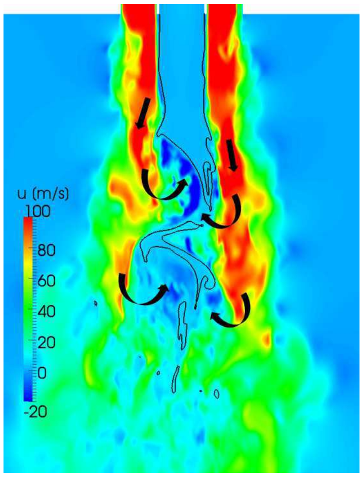

FIG. 9. Contours of instantaneous streamwise velocity and $f = 0.5$ iso-surface illustrating the breakup mechanism of liquid core through aerodynamic interference.

Figure 10 illustrates contours of calculated time-averaged velocity (top) as well as their root mean squared fluctua-

Accepted to Phys. Fluids 10.1063/5.0141156

tions (bottom) on a cutting plane passing through the centerline axis, with the solid lines representing the time-mean iso-surfaces of $\bar{f} = 0.5$. Both $\bar{u}$ and u' yield self-similar distributions for the up-scaled nozzles. Overall, u' is large along the shear layers and is at its largest near the tip of the liquid jet, where unsteady breakup of the liquid jet leads to strong fluctuations of the local flow velocity. $\bar{u}$ decreases for up-scaled nozzles, which is in accordance with the theoretical analysis shown in Eq. 7. The same behavior can be detected for u', which decreases with $\dot{M}_{liq}$ due to the decreased gas flow velocity or the weakened velocity gradient at the gas-liquid interface, respectively. A decrease of u' indicates less intense turbulent fluctuations, so that the multiphase momentum transfer is attenuated. As a result, atomization performance is worsened while up-scaling $\dot{M}_{liq}$, leading to a decreased breakup length. The results reveal that, in addition to the commonly used time mean flow velocity, the turbulence intensity in terms of u' represents a reasonable measure for the breakup performance, which dominates the multiphase interactions. An improved atomization performance can be achieved by more intense turbulent fluctuations.

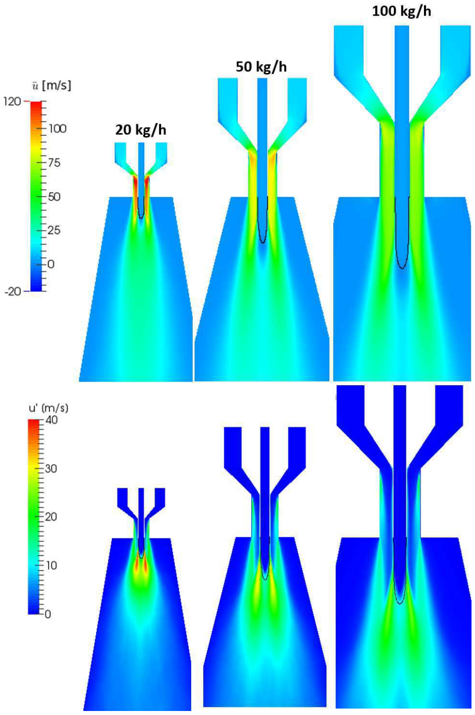

FIG. 10. Contours of time-mean streamwise velocity $\bar{u}$ and root mean squared (rms) values of velocity fluctuations u' calculated by VOF-LES for up-scaled nozzles.

3. Liquid phase kinetic energy

In order to further reveal the dynamic behavior of the breakup process during nozzle up-scaling, the volume-specific kinetic energy of the liquid phase k_L has been evaluated from the simulations

$$k_L = \frac{K_L}{V_L} = \frac{\int_V k_f \, \mathrm{d}V}{\int_V f \, \mathrm{d}V} \quad \text{in} \quad [\mathrm{J/m_L^3}] \tag{23}$$

where the specific kinetic energy of the liquid averaged over the cell volume k_f is calculated from

$$k_f = f \cdot \frac{1}{2} \rho_L \mathbf{u}_L^2 \quad \text{in} \quad [\mathrm{J/m^3}] \tag{24}$$

with the velocity of the liquid phase $\mathbf{u}_L$ evaluated by

$$\mathbf{u}_L = \mathbf{u} + (1 - f)\, \mathbf{u}_r \tag{25}$$

K_L and V_L in Eq. 23 are evaluated from volume integration of k_f and f over the whole computational domain, which measures the total kinetic energy and volume of the liquid phase. Therefore, k_L represents an integral quantity for the attained kinetic energy per unit liquid volume. As k_L of the liquid stream issuing from the nozzle remains constant while up-scaling $\dot{M}_{liq}$ due to the use of a constant v_{liq}, i.e., $k_{L,0} = \rho_L u_L^2/2$, an increase of k_L denotes specifically a more intense multiphase momentum exchange.

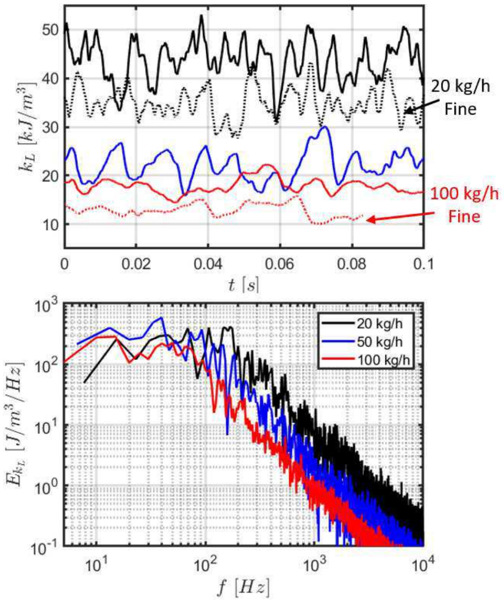

FIG. 11. Temporal development (top) and spectral distributions (bottom) of calculated specific kinetic energy in the liquid phase k_L.

Physics of Fluids ACCEPTED MANUSCRIPT

This is the author's peer reviewed, accepted manuscript. However, the online version of record will be different from this version once it has been copyedited and typeset.
PLEASE CITE THIS ARTICLE AS DOI: 10.1063/5.0141156

AIP Publishing

Figure 11 depicts the calculated temporal progression of k_L (top) and its spectral distributions (bottom) evaluated from FFT (Fast Fourier Transformation) of the time series of k_L at different mass flows. As shown in the upper part of Fig. 11, k_L yields a strong time fluctuation due to the unsteady nature of the breakup process. The time-mean value of k_L decreases with the degree of up-scaling, which is in accordance with the decreased $\bar{u}$ and u', as shown in Fig. 10. The difference is larger while comparing k_L from 20 and 50 kg/h than that from 50 to 100 kg/h, which is attributed to the more strongly increased n from 20 to 50 kg/h than that from 50 to 100 kg/h, which leads to a stronger decrease of the characteristic parameters like u_{gas}, u', j as well as k_L with n in a non-linear way. The dotted lines shown in Fig. 11 at the top indicate simulation results for the 20 kg/h and 100 kg/h nozzles using twice-refined grids, revealing a decreased k_L with increased grid resolution. In this case, more small-scale liquid fragments downstream can be resolved and the resolved liquid phase volume V_L increases due to the reduced numerical diffusion, leading to a decrease of k_L.

The same behavior with a decrease of k_L with n is also confirmed for the spectra of k_L or E_{k_L} shown in the lower part of Fig. 11, which decreases with increased $\dot{M}_{liq}$ and, therefore, yields a positive correlation with u'. E_{k_L} represents a measure of the fluctuation amplitude of k_L at a given frequency and it yields a broadband distribution in the frequency domain. In addition, E_{k_L} yields a similar shape compared with the spectrum of the turbulence kinetic energy (TKE) for a general turbulent flow. The result reveals that the transfer mechanism of momentum or kinetic energy from the gas to the liquid phase is dominated by the turbulent flow fluctuations.

4. *Kelvin-Helmholtz frequency*

During the initial stage of the breakup process, surface waves are generated on the liquid jet due to the Kelvin-Helmholtz instability (KHI) caused by the velocity difference between the liquid and gas flows. These interfacial waves develop further periodically and transfer momentum or kinetic energy downstream, until primary liquid ligaments pinch-off from the intact jet core. For the glycerol/water mixture with a high viscosity, the KHI wave formations can be detected clearly from the high-speed images, which are illustrated in Fig. 12 along with snapshots of calculated iso-surfaces of $f = 0.5$ obtained from the simulations for $\dot{M}_{liq} = 50$ kg/h. The arrows in Fig. 12 indicate instantaneous peaks of the KHI waves.

The characteristic frequencies f_{KHI} have been evaluated for varying $\dot{M}_{liq}$ and We_{aero} and are depicted in Fig. 13. The measured and calculated f_{KHI} yield a reasonably good agreement with the estimation by applying theoretical analysis[7,11,45]. An increase in We_{aero} leads to an increase of f_{KHI}, which is due to the faster motion of KHI waves at higher gas velocity. An increase in $\dot{M}_{liq}$ or nozzle scale causes a decrease of f_{KHI}, which can be explained by the decreased gas velocity (see Eq. 7) and momentum flux ratio (see Eq. 10) at constant We_{aero}. Similar behavior has also been reported in[46], where f_{KHI} increases while up-scaling the nozzle at constant v_{gas} and v_{liq}. The correlation between f_{KHI} and We_{aero} is given in Eq. 12-14 in terms of the gas velocity, which reveals an increase of f_{KHI} with We_{aero}. This correlation results from instability theory according to Dimotakis[36] and Marmottant and Villermaux[7], which was originally developed for low viscous liquids such as water. For fluids with increased viscosities, a proportionality factor $X = 0.1$ has been implemented in Eq. 12 as proposed in Sänger et al.[6], which accounts for the damping effect of flow stretch caused by the increased liquid viscosity.

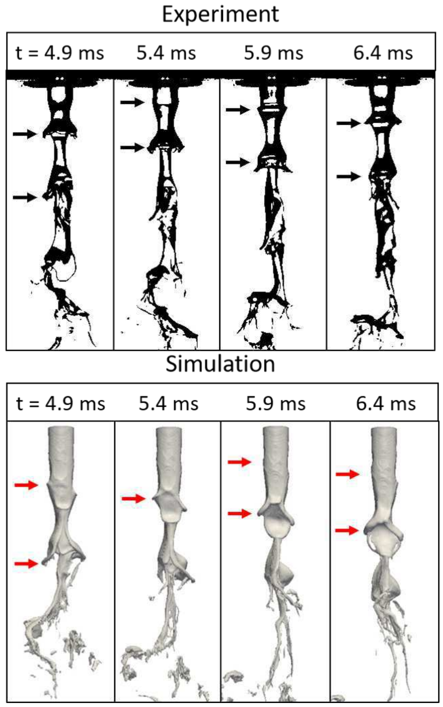

FIG. 12. Comparison between high-speed camera images and simulation results of the KHI wave at $\dot{M}_{liq}$ = 50 kg/h and We_{aero} = 250 for individual time steps.

C. Discussions

The objective of the current work is to study the behavior of primary atomization for up-scaled nozzles in terms of increasing the liquid mass flow rate, where the challenge is given by scaling up the nozzle while not changing the atomization or spray quality. Due to the chosen approach of keeping We_{aero} and GLR constant, u_{gas} decreases and Re_{liq} increases for up-scaled nozzles, which leads to a worsened atomization performance. Another approach concerning an improved atom-

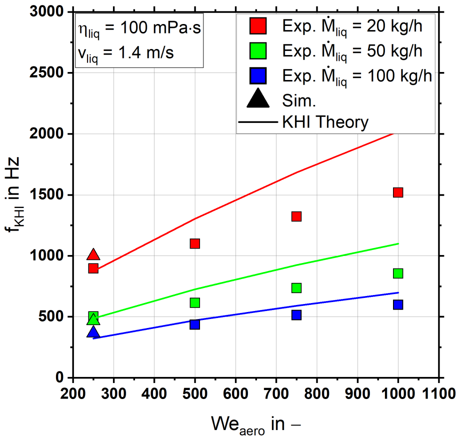

FIG. 13. KHI wave frequency in dependence of We_{aero} for $\dot{M}_{liq}$ = 20, 50, 100 kg/h at η_{liq} = 100 mPa·s extracted from the experiments, simulations and instability theory.

ization behavior is to increase u_{gas} or GLR while up-scaling the nozzle. However, this is not desired concerning an optimal product yield in thermo-chemical conversion processes. In fact, as GLR, We_{aero}, Re_{liq} and j are interrelated with each other via the flow conditions, it is impossible to keep all these parameters constant while up-scaling the nozzle. For instance, GLR and We_{aero} will be changed inevitably with n, if the same u_{gas} or j is used. In contrast, keeping GLR and We_{aero} constant will lead to variations of u_{gas}, Re_{liq} and j, as employed in the current work.

The results reveal that it is not enough to use solely constant We_{aero} in order to have the same atomization behavior for up-scaled nozzles with proportionally increased mass flows. However, the pulsating-type breakup regime remains unchanged for different nozzle scales, which follows the general classification of breakup regimes proposed by Faragò and Chigier[2] based on We_{aero} and Re_{liq}. As discussed in the review work by Dumouchel[8], the breakup length L_C can be correlated with the other dimensionless parameters like the gas-to-liquid momentum flux ratio j. In addition, nozzle design parameters, flow patterns within the nozzle nozzle emerging from upstream conditions and even the relative inclination angles can have a strong impact on L_C[27].

The current study has been conducted under atmospheric conditions. An alternative approach to increase the mass flow rate is to conduct the atomization process at elevated pressures. The influence of ambient pressure was investigated in previous works[9,30,47]. In general, the system pressure plays a major role for liquid jet breakup as well as the resulting droplet size. An increased pressure leads to a higher We_{aero} and j due to the increased gas-to-liquid density ratio, which results in a reinforced multiphase momentum transfer and a more intensified breakup process[47]. This work has shown that at atmospheric pressure or given density ratio, up-scaling the nozzle at constant We_{aero} and GLR will cause an increase of L_C due to the decrease of u_{gas} and j. At elevated pressure, the density ratio remains constant while up-scaling the nozzle, so that the same behavior applies for elevated pressure conditions, too.

V. CONCLUSIONS

Experiments and accompanying numerical simulations have been carried out in order to study the primary breakup process of liquid jets from coaxial, gas-assisted atomizers in different mass flow scales. An approach to proportionally modulate the nozzle dimensions at constant aerodynamic Weber number We_{aero} and gas-to-liquid ratio GLR was chosen. Water as well as a glycerol/water mixture with viscosity of 1 and 100 mPa·s were used and the mass flow rate of the liquid $\dot{M}_{liq}$ has been scaled from 20 to 500 kg/h at We_{aero} = 250, 500, 750 and 1000 for the experiments. Numerical simulations were performed for $\dot{M}_{liq}$ = 20, 50, 100 kg/h at $We_{aero} = 250$.

In summary, the experiments revealed an increase of the breakup length L_C, a decrease in KHI frequency f_{KHI}, as well as a decrease in the droplet number density with up-scaled $\dot{M}_{liq}$ or nozzle size at constant We_{aero} and GLR. The same findings have been confirmed by the numerical simulations and further analysis regarding the dynamic behavior of the turbulent gas flow and liquid jet during the breakup process has indicated a decrease of relative flow velocity, turbulent fluctuations and specific kinetic energy in the liquid phase with up-scaled $\dot{M}_{liq}$, leading to an attenuated multiphase momentum transfer. Therefore, increasing $\dot{M}_{liq}$ by up-scaling the nozzle geometry worsens the atomization performance, even though We_{aero} is kept constant. In addition, the kinetic energy from the liquid phase has been found to be characterized by a cascade-like distribution in the spectral domain, similar to that of the turbulent gas flow.

In conclusion, special attention should be given to designing high-load gas-assisted, co-axial atomizer based on up-scaling the nozzles developed at laboratory-scale. The proposed correlations of L_C with the factor of mass flow scaling n may be used as a first-order estimate for predicting behaviors of the primary breakup process, where the impact of n can be incorporated into j and Re_{liq} by using Eq. 9 and 11.

ACKNOWLEDGMENTS

The authors gratefully acknowledge the financial support by the Helmholtz Association of German Research Centers (HGF), within the research field MTET (Materials and Technologies for the Energy Transition), subtopic "Anthropogenic Carbon Cycle" (38.05.01). This work utilized computing resources provided by the High Performance Computing Center Stuttgart (HLRS) and the Steinbuch Centre for Computing (SCC) at the Karlsruhe Institute of Technology.

[1] L. Bayvel and Z. Orzechowski, *Liquid Atomization* (Taylor & Francis, Washington, DC, 1993).

Accepted to Phys. Fluids 10.1063/5.0141156

[2] N. Chigier and Z. Faragó, "Morphological classification of disintegration of round liquid jets in a coaxial air stream," At. Sprays **2**, 137–153 (1992).

[3] J. C. Lasheras and E. J. Hopfinger, "Liquid jet instability and atomization in a coaxial gas stream," Annu. Rev. Fluid Mech. **32**, 275–308 (2000).

[4] H. Zhao, H.-F. Liu, J.-L. Xu, W.-F. Li, and W. Cheng, "Breakup and atomization of a round coal water slurry jet by an annular air jet," Chem. Eng. Sci. **78**, 63–74 (2012).

[5] A. Sänger, T. Jakobs, N. Djordjevic, and T. Kolb, "Experimental investigation on the influence of ambient pressure on twin-fluid atomization of liquids with various viscosities," ICLASS (2015).

[6] A. Sänger, T. Jakobs, and T. Kolb, "Using primary instability analysis for determination of apparent liquid viscosity at jet breakup atomizing non-newtonian fluids," 27th Annual Conference on Liquid Atomization and Spray Systems (2016).

[7] P. Marmottant and E. Villermaux, "On spray formation," J. Fluid Mech. **498**, 73–111 (2004).

[8] C. Dumouchel, "On the experimental investigation on primary atomization of liquid streams," Exp Fluids **45**, 371–422 (2008).

[9] S. Wachter, T. Jakobs, and T. Kolb, "Towards system pressure scaling of gas assisted coaxial burner nozzles – an empirical model," Appl. Energy Combust. Sci. **5**, 100019 (2021).

[10] H. Schlichting, K. Gersten, and E. Krause, *Grenzschicht-Theorie: Mit 22 Tabellen*, 10th ed. (Springer-Verlag Berlin Heidelberg, Berlin, Heidelberg, 2006).

[11] A. Kumar and S. Sahu, "Influence of nozzle geometry on primary and large-scale instabilities in coaxial injectors," Chem. Eng. Sci. **221**, 1–18 (2020).

[12] N. Machicoane, G. Ricard, R. Osuna-Orozco, P. D. Huck, and A. Aliseda, "Influence of steady and oscillating swirl on the near-field spray characteristics in a two-fluid coaxial atomizer," Int. J. Multiph. Flow **129**, 103318 (2020).

[13] J. K. Bothell, N. Machicoane, D. Li, T. B. Morgan, A. Aliseda, A. L. Kastengren, and T. J. Heindel, "Comparison of x-ray and optical measurements in the near-field of an optically dense coaxial air-assisted atomizer," Int. J. Multiph. Flow **125**, 103219 (2020).

[14] B. Leroux, O. Delabroy, and F. Lacas, "Experimental study of coaxial atomizers scaling. part 1: Dense core zone," At. Sprays **17**, 381–407 (2007).

[15] B. Leroux, O. Delabroy, and F. Lacas, "Experimental study of coaxial atomizers scaling. part 2: Diluted zone," At. Sprays **17**, 409–430 (2007).

[16] F. Xiao, M. Dianat, and J. J. McGuirk, "Les of turbulent liquid jet primary breakup in turbulent coaxial air flow," Int. J. Multiph. Flow **60**, 103–118 (2014).

[17] M. Gorokhovski and M. Herrmann, "Modeling primary atomization," Annu. Rev. Fluid Mech. **40**, 343–366 (2008).

[18] J. Shinjo and A. Umemura, "Simulation of liquid jet primary breakup: Dynamics of ligament and droplet formation," Int. J. Multiph. Flow **36**, 513–532 (2010).

[19] A. Zandian, W. A. Sirignano, and F. Hussain, "Planar liquid jet: Early deformation and atomization cascades," Phys. Fluids **29**, 062109 (2017).

[20] V. Srinivasan, A. J. Salazar, and K. Saito, "Modeling the disintegration of modulated liquid jets using volume-of-fluid (vof) methodology," Appl. Math. Model. **35**, 3710–3730 (2011).

[21] B. Duret, J. Reveillon, T. Menard, and F. X. Demoulin, "Improving primary atomization modeling through dns of two-phase flows," Int. J. Multiph. Flow **55**, 130–137 (2013).

[22] H. Grosshans, A. Movaghar, L. Cao, M. Oevermann, R.-Z. Szász, and L. Fuchs, "Sensitivity of vof simulations of the liquid jet breakup to physical and numerical parameters," Comput. Fluids **136**, 312–323 (2016).

[23] T. Müller, A. Sänger, P. Habisreuther, T. Jakobs, D. Trimis, T. Kolb, and N. Zarzalis, "Simulation of the primary breakup of a high-viscosity liquid jet by a coaxial annular gas flow," Int. J. Multiph. Flow **87**, 212–228 (2016).

[24] M. Saeedipour, S. Pirker, S. Bozorgi, and S. Schneiderbauer, "An eulerian–lagrangian hybrid model for the coarse-grid simulation of turbulent liquid jet breakup," Int. J. Multiph. Flow **82**, 17–26 (2016).

[25] F. Zhang, T. Zirwes, T. Müller, S. Wachter, T. Jakobs, P. Habisreuther, N. Zarzalis, D. Trimis, and T. Kolb, "Effect of elevated pressure on air-assisted primary atomization of coaxial liquid jets: Basic research for entrained flow gasification," Renew. Sustain. Energy Rev. **134**, 110411 (2020).

[26] K. Warncke, S. Gepperth, B. Sauer, A. Sadiki, J. Janicka, R. Koch, and H.-J. Bauer, "Experimental and numerical investigation of the primary breakup of an airblasted liquid sheet," Int. J. Multiph. Flow **91**, 208–224 (2017).

[27] F. Zhang, T. Zirwes, S. Wachter, T. Jakobs, P. Habisreuther, N. Zarzalis, D. Trimis, T. Kolb, H. Bockhorn, and D. Stapf, "Numerical simulations of air-assisted primary atomization at different air-to-liquid injection angles," Int. J. Multiph. Flow **158**, 104304 (2023).

[28] S. Wachter, T. Jakobs, and T. Kolb, "Mass flow scaling of gas-assisted coaxial atomizers," Appl. Sci. **12** (2022), 10.3390/app12042123.

[29] T. Müller, P. Habisreuther, N. Zarzalis, A. Sänger, T. Jakobs, and T. Kolb, "Investigation on jet breakup of high-viscous fuels for entrained flow gasification," in *Proceedings of the ASME Turbo Expo: Turbine Technical Conference and Exposition - 2016* (The American Society of Mechanical Engineers, New York, N.Y., 2016).

[30] S. Wachter, T. Jakobs, and T. Kolb, "Experimental investigation on the influence of system pressure on resulting spray quality and jet breakup applying pressure adapted twin-fluid nozzles," Int. J. Multiph. Flow **125**, 103189 (2020).

[31] S. Wachter, T. Jakobs, and T. Kolb, "Effect of solid particles on droplet size applying the time-shift method for spray investigation," Appl. Sci. **10**, 7615 (2020).

[32] S. Wachter, T. Jakobs, and T. Kolb, "Comparison of central jet and annular sheet atomizers at identical gas momentum flows," Ind. Eng. Chem. Res. **60**, 11502–11512 (2021).

[33] N. Otsu, "A threshold selection method from gray-level histograms," IEEE Transactions on Systems, Man, and Cybernetics **9**, 62–66 (1979).

[34] J. Kapur, P. Sahoo, and A. Wong, "A new method for gray-level picture thresholding using the entropy of the histogram," Comput. Gr. Image Process. **29**, 273–285 (1985).

[35] M. Versluis, "High-speed imaging in fluids," Exp. Fluids **54**, 1–35 (2013).

[36] P. E. Dimotakis, "Two-dimensional shear-layer entrainment," AIAA journal **24**, 1791–1796 (1986).

[37] L. Bernal and A. Roshko, "Streamwise vortex structure in plane mixing layers," J. Fluid Mech. **170**, 499–525 (1986).

[38] H. Rusche, "Computational fluid dynamics of dispersed two-phase flows at high phase fractions," Mater. Sci. (2003).

[39] S. M. Damian, "Description and utilization of interfoam multiphase solver," (2012).

[40] J. Fröhlich, *Large Eddy Simulation turbulenter Strömungen* (Teubner, Wiesbaden, 2006).

[41] J. Brackbill, D. Kothe, and C. Zemach, "A continuum method for modeling surface tension," J. Comput. Phys. **100**, 335–354 (1992).

[42] A. Albadawi, D. Donoghue, A. Robinson, D. Murray, and Y. Delauré, "Influence of surface tension implementation in volume of fluid and coupled volume of fluid with level set methods for bubble growth and detachment," Int. J. Multiph. Flow **53**, 11–28 (2013).

[43] P. Liovic and D. Lakehal, "Subgrid-scale modelling of surface tension within interface tracking-based large eddy and interface simulation of 3d interfacial flows," Comput. Fluids **63**, 27–46 (2012).

[44] "OpenFOAM: The open source cfd toolbox," (2018).

[45] A. Kumar and S. Sahu, "Liquid jet breakup unsteadiness in a coaxial air-blast atomizer," Int. J. Spray Combust. Dyn. **17**, 175682771876090 (2018).

[46] X.-S. Tian, H. Zhao, H.-F. Liu, W.-F. Li, and J.-L. Xu, "Effect of central tube thickness on wave frequency of coaxial liquid jet," Fuel Process. Technol. **119**, 190–197 (2014).

[47] Z. Zhang and S. Ziada, "PDA measurements of droplet size and mass flux in the three-dimensional atomisation region of water jet in air cross-flow," Exp. Fluids **28**, 29–35 (2000).

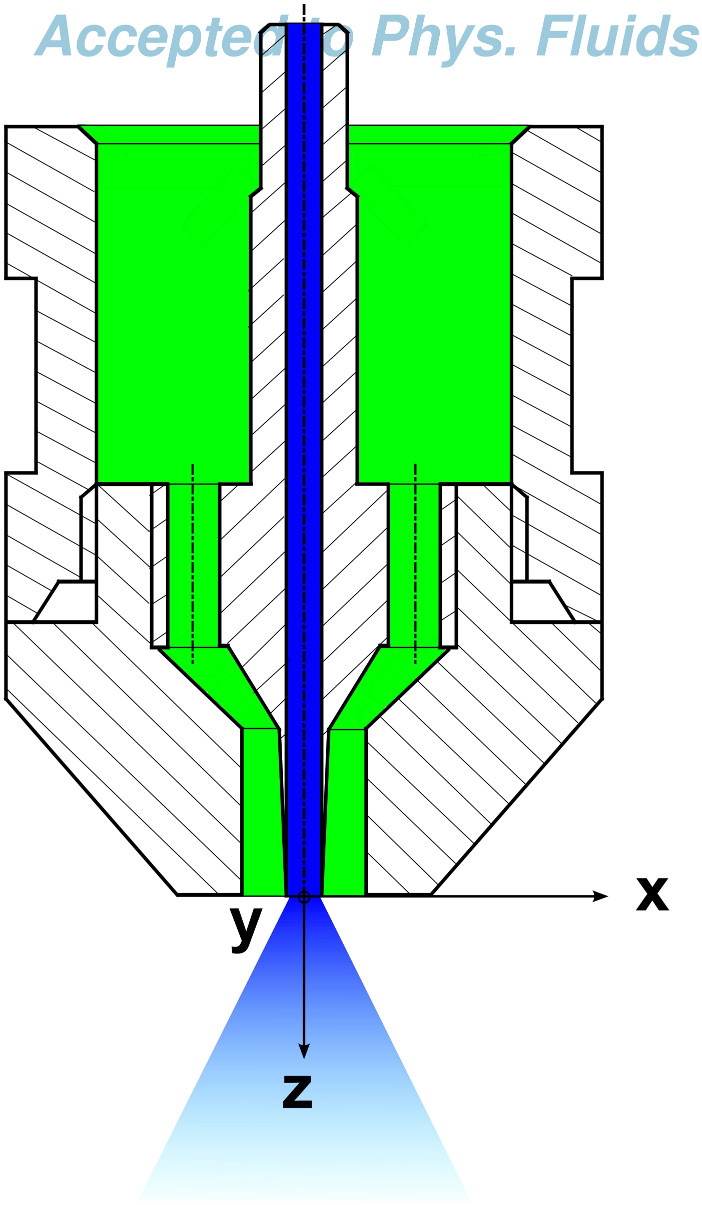
x
y
z

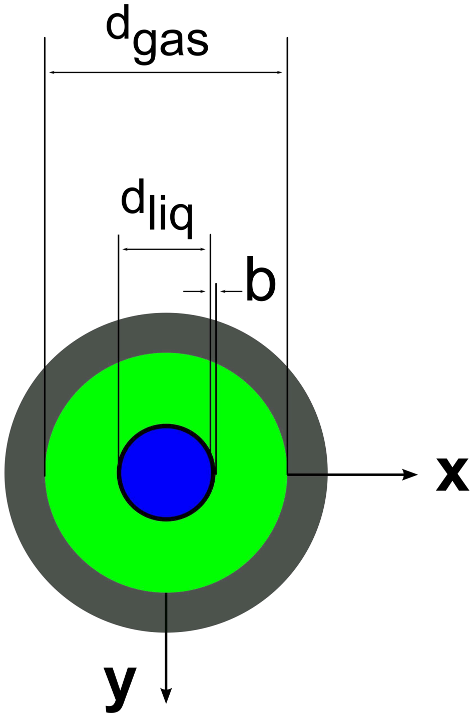
d_{gas}
d_{liq}
b
x
y

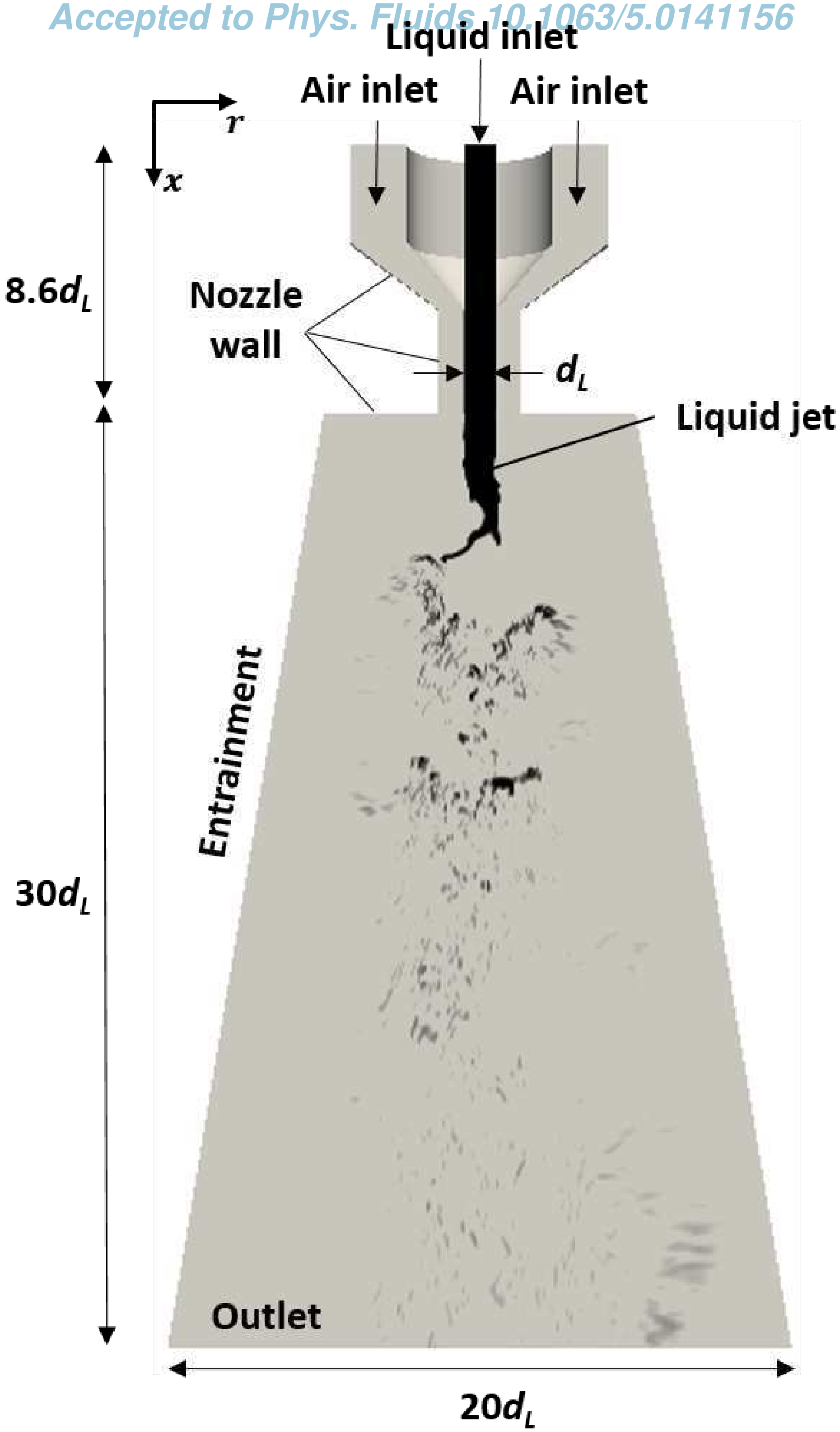
Liquid inlet
Air inlet
Air inlet
r
x
8.6d_L
Nozzle wall
d_L
Liquid jet
Entrainment
30d_L
Outlet
20d_L

AIP Publishing Physics of Fluids ACCEPTED MANUSCRIPT

This is the author's peer reviewed, accepted manuscript. However, the online version of record will be different from this version once it has been copyedited and typeset.

PLEASE CITE THIS ARTICLE AS DOI: 10.1063/5.0141156

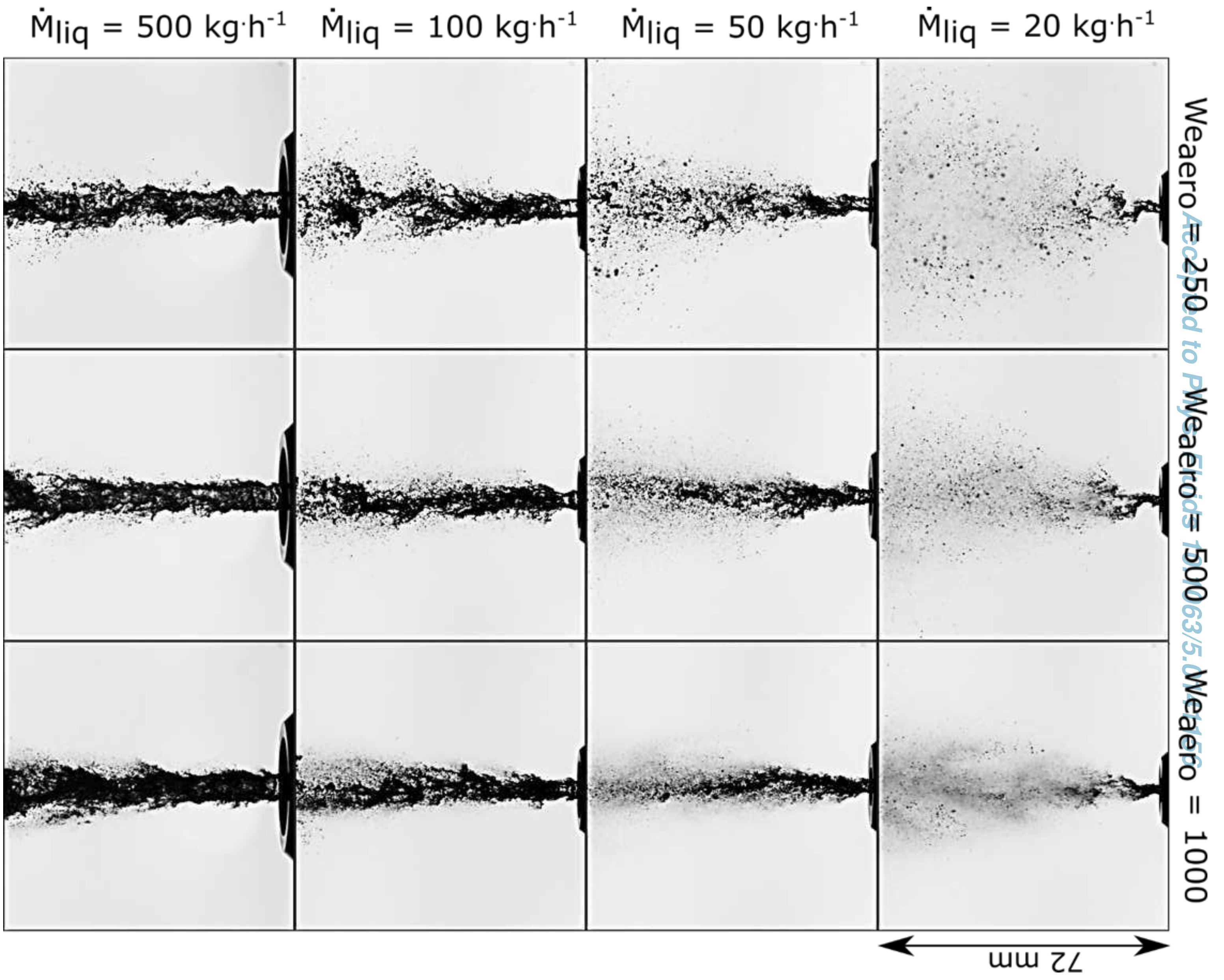
$\dot{M}_{liq}$ = 500 kg·h^{-1}
$\dot{M}_{liq}$ = 100 kg·h^{-1}
$\dot{M}_{liq}$ = 50 kg·h^{-1}
$\dot{M}_{liq}$ = 20 kg·h^{-1}
We$_{aero}$ = 250
We$_{aero}$ = 500
We$_{aero}$ = 1000
72 mm

AIP Publishing Physics of Fluids ACCEPTED MANUSCRIPT

This is the author's peer reviewed, accepted manuscript. However, the online version of record will be different from this version once it has been copyedited and typeset.

PLEASE CITE THIS ARTICLE AS DOI: 10.1063/5.0141156

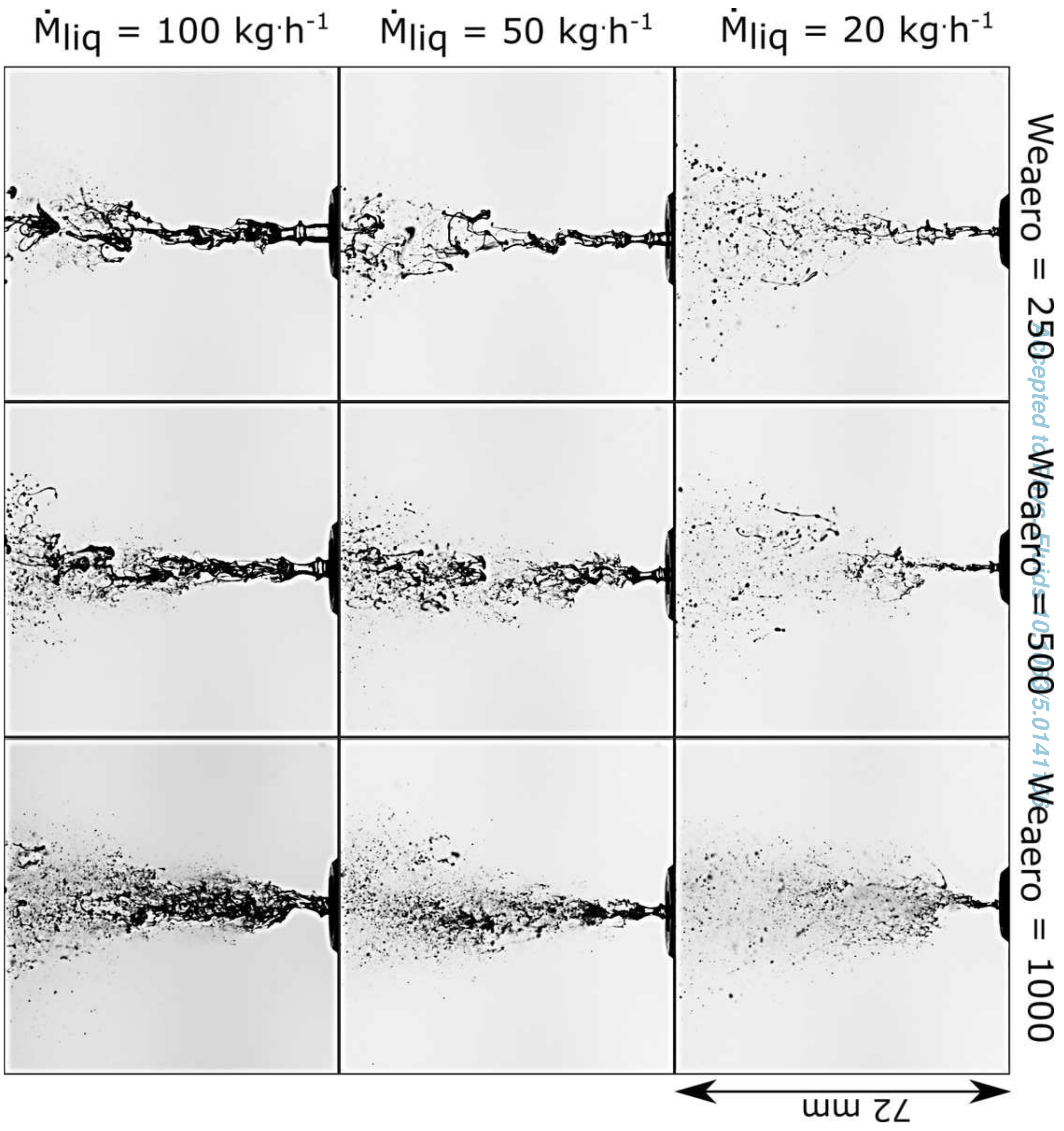
$We_{aero} = 250$
$We_{aero} = 500$
$We_{aero} = 1000$
$\dot{M}_{liq} = 20\ kg{\cdot}h^{-1}$
$\dot{M}_{liq} = 50\ kg{\cdot}h^{-1}$
$\dot{M}_{liq} = 100\ kg{\cdot}h^{-1}$
72 mm

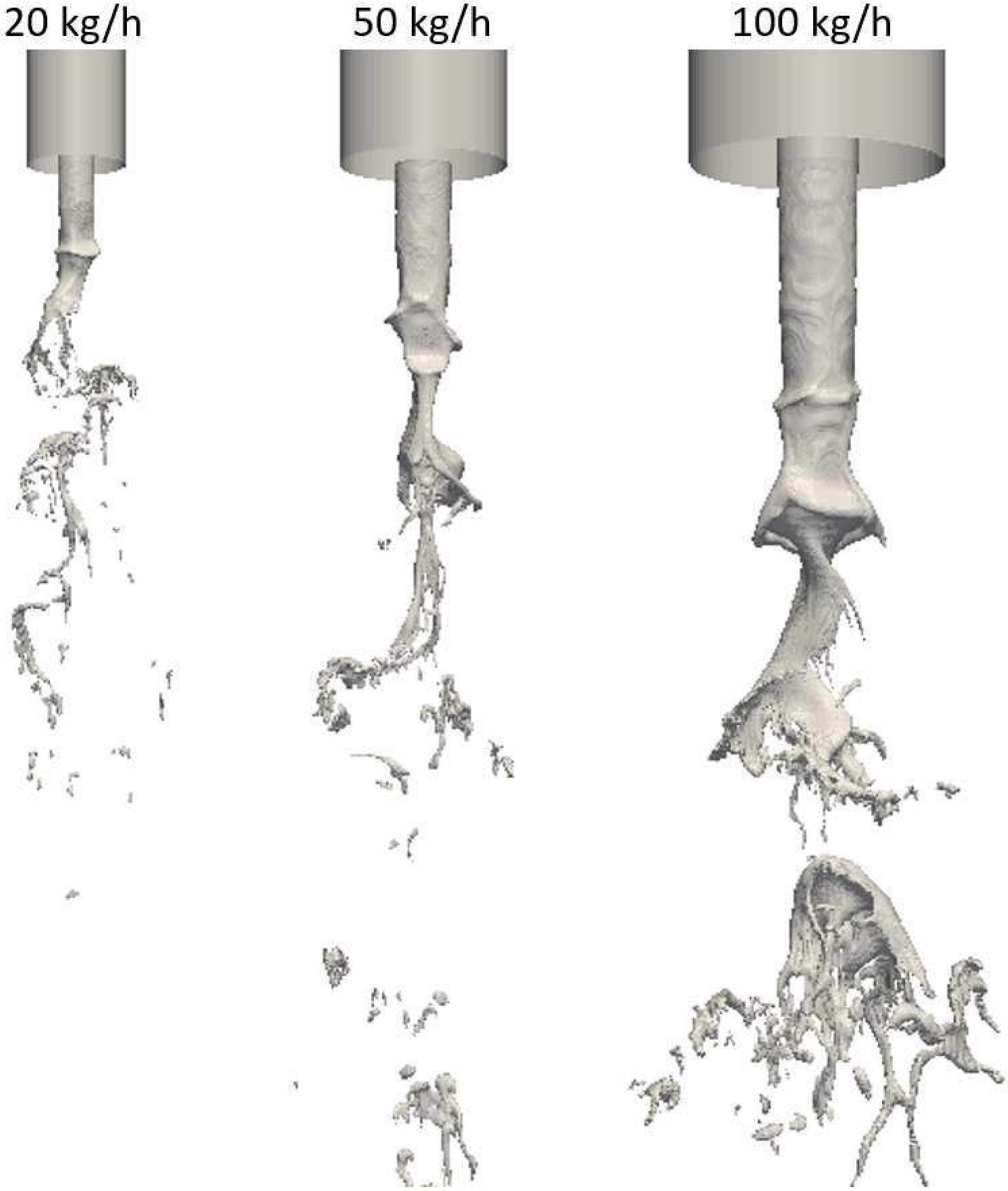
20 kg/h
50 kg/h
100 kg/h

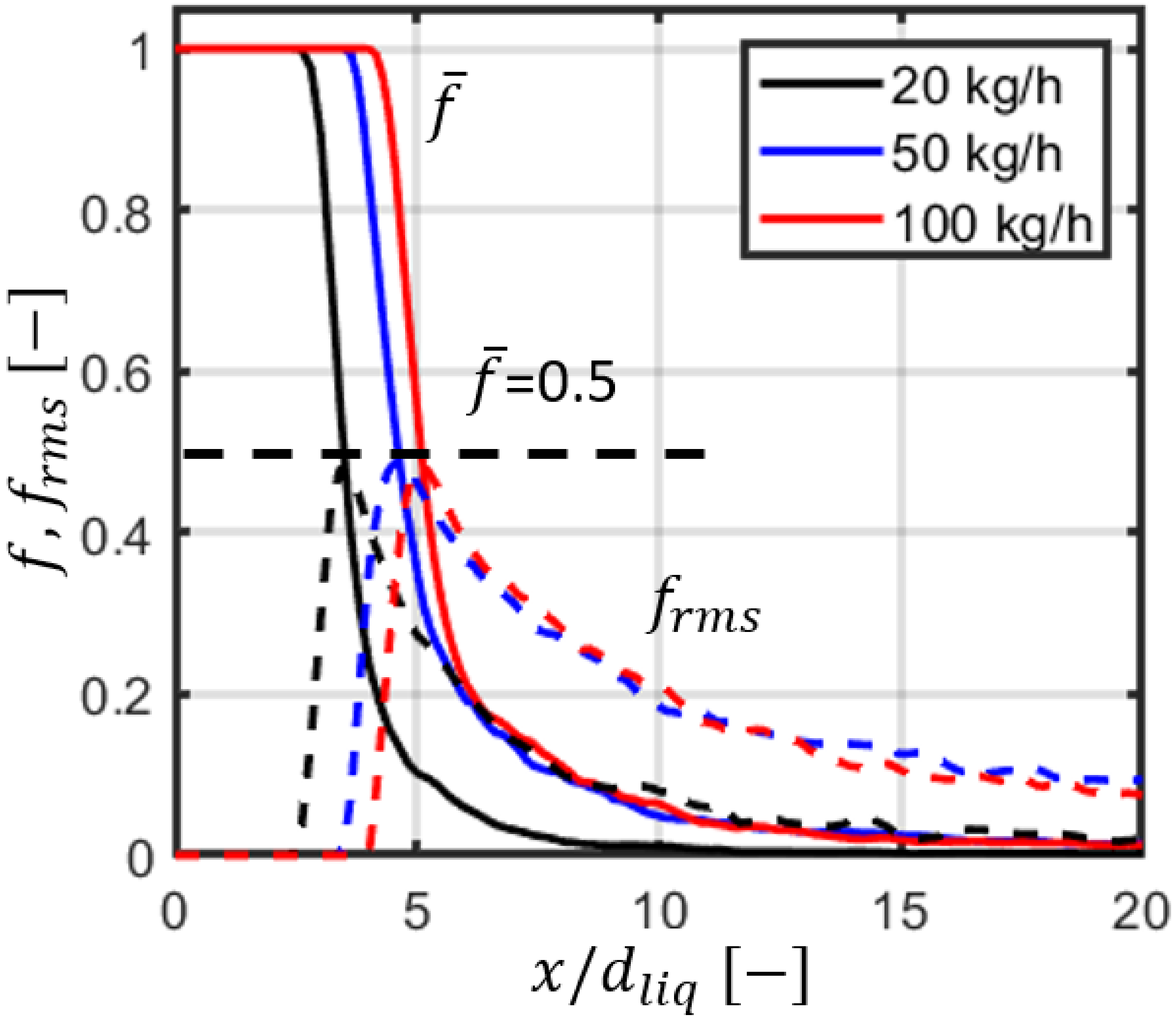
$\bar{f}$
$\bar{f}$=0.5
f_{rms}
20 kg/h
50 kg/h
100 kg/h
f, f_{rms} [−]
1
0.8
0.6
0.4
0.2
0
0
5
10
15
20
x/d_{liq} [−]

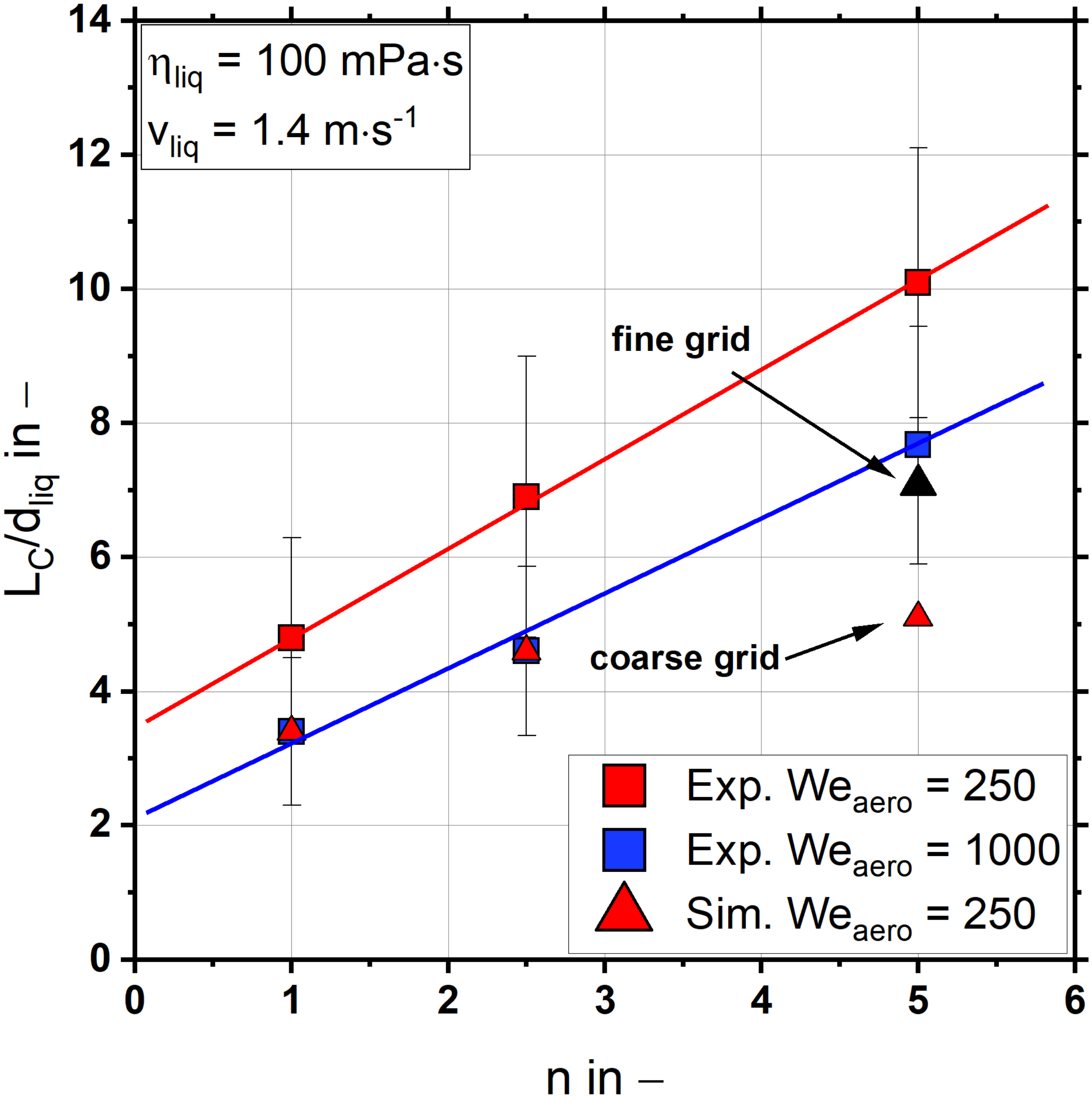
η_{liq} = 100 mPa·s
v_{liq} = 1.4 m·s^{-1}
fine grid
coarse grid
Exp. We_{aero} = 250
Exp. We_{aero} = 1000
Sim. We_{aero} = 250
L_C/d_{liq} in –
n in –
0
2
4
6
8
10
12
14
0
1
2
3
4
5
6

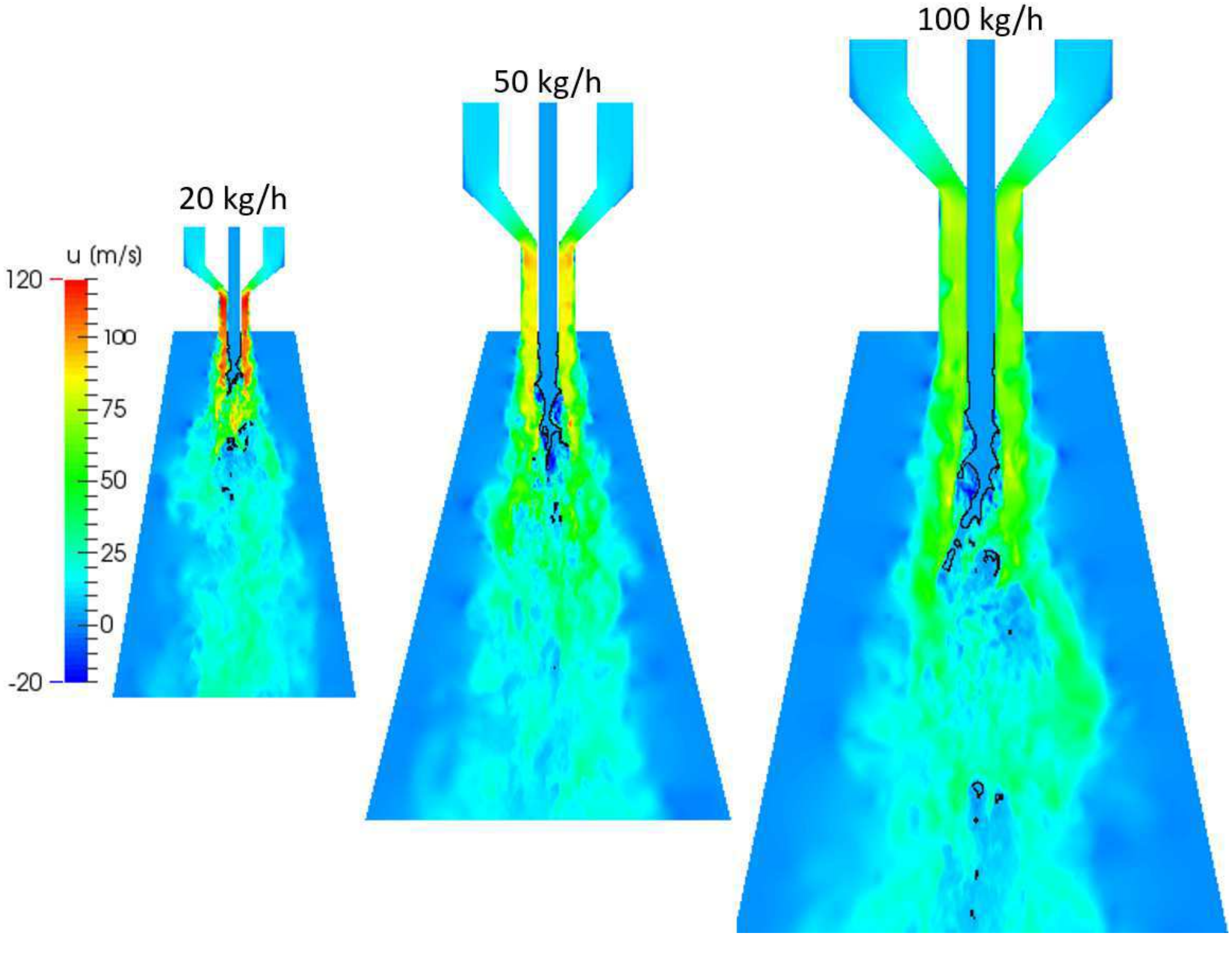
20 kg/h
50 kg/h
100 kg/h
u (m/s)
120
100
75
50
25
0
-20

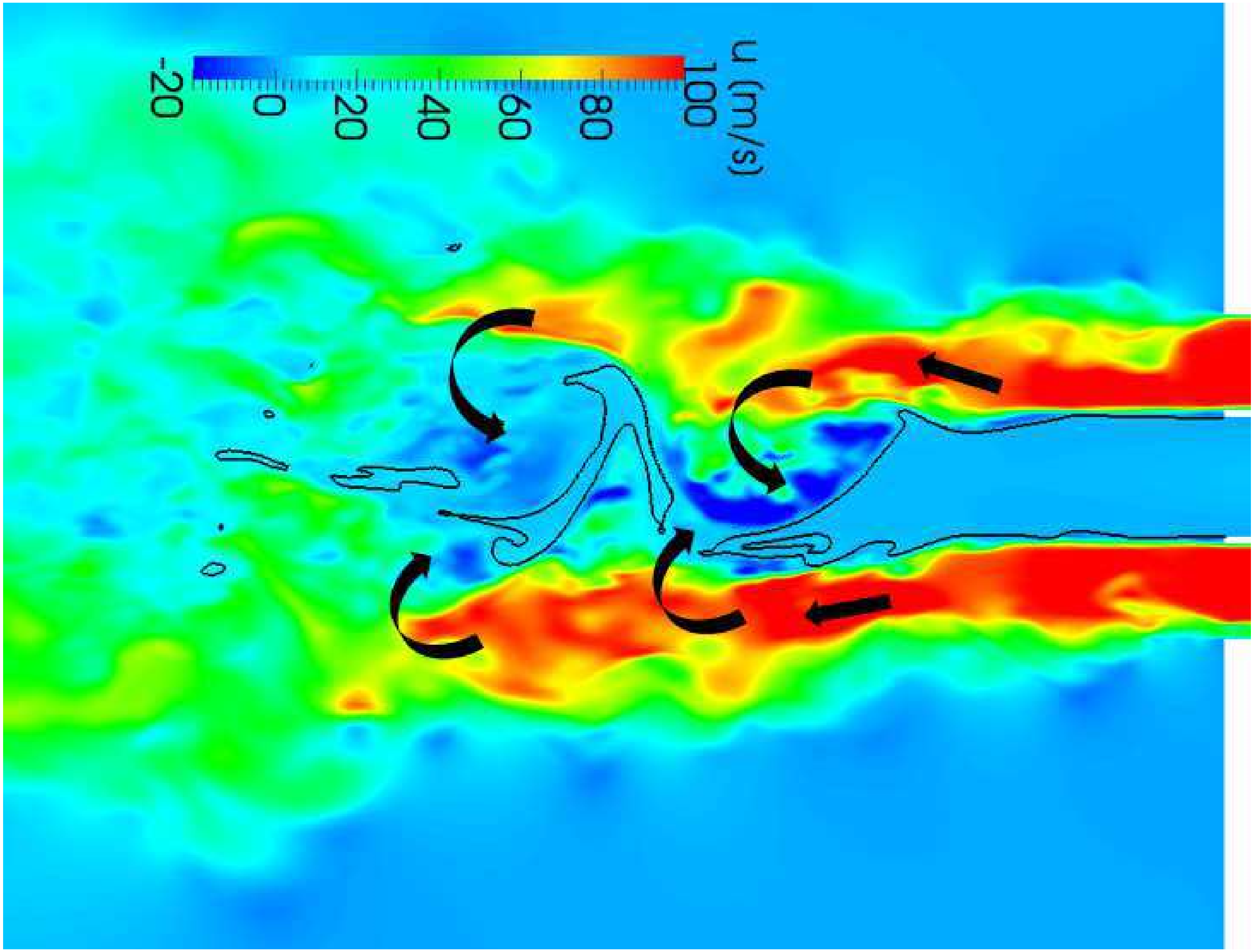
u (m/s)
100
80
60
40
20
0
-20

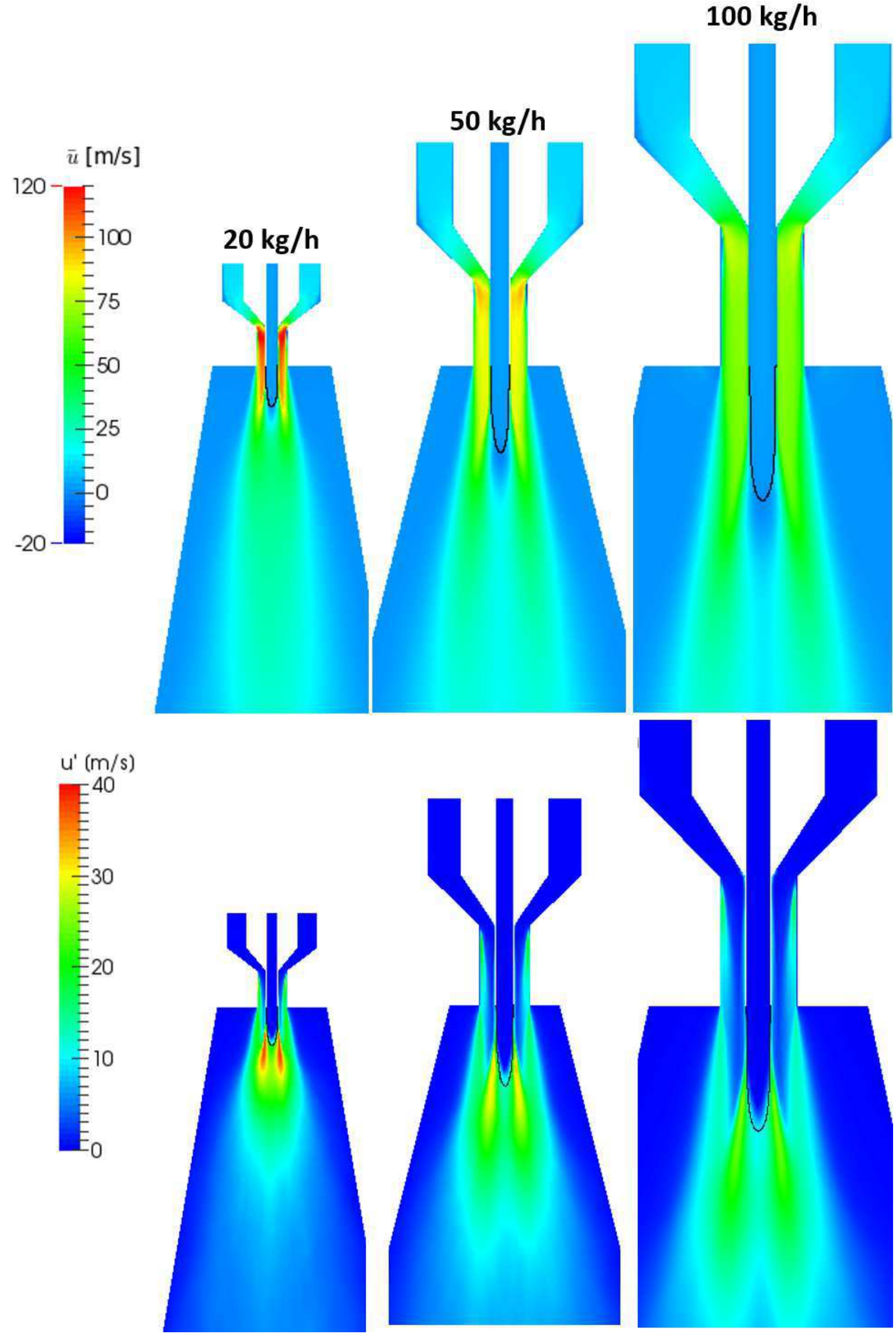
100 kg/h
50 kg/h
20 kg/h
$\bar{u}$ [m/s]
120
100
75
50
25
0
-20
u' (m/s)
40
30
20
10
0

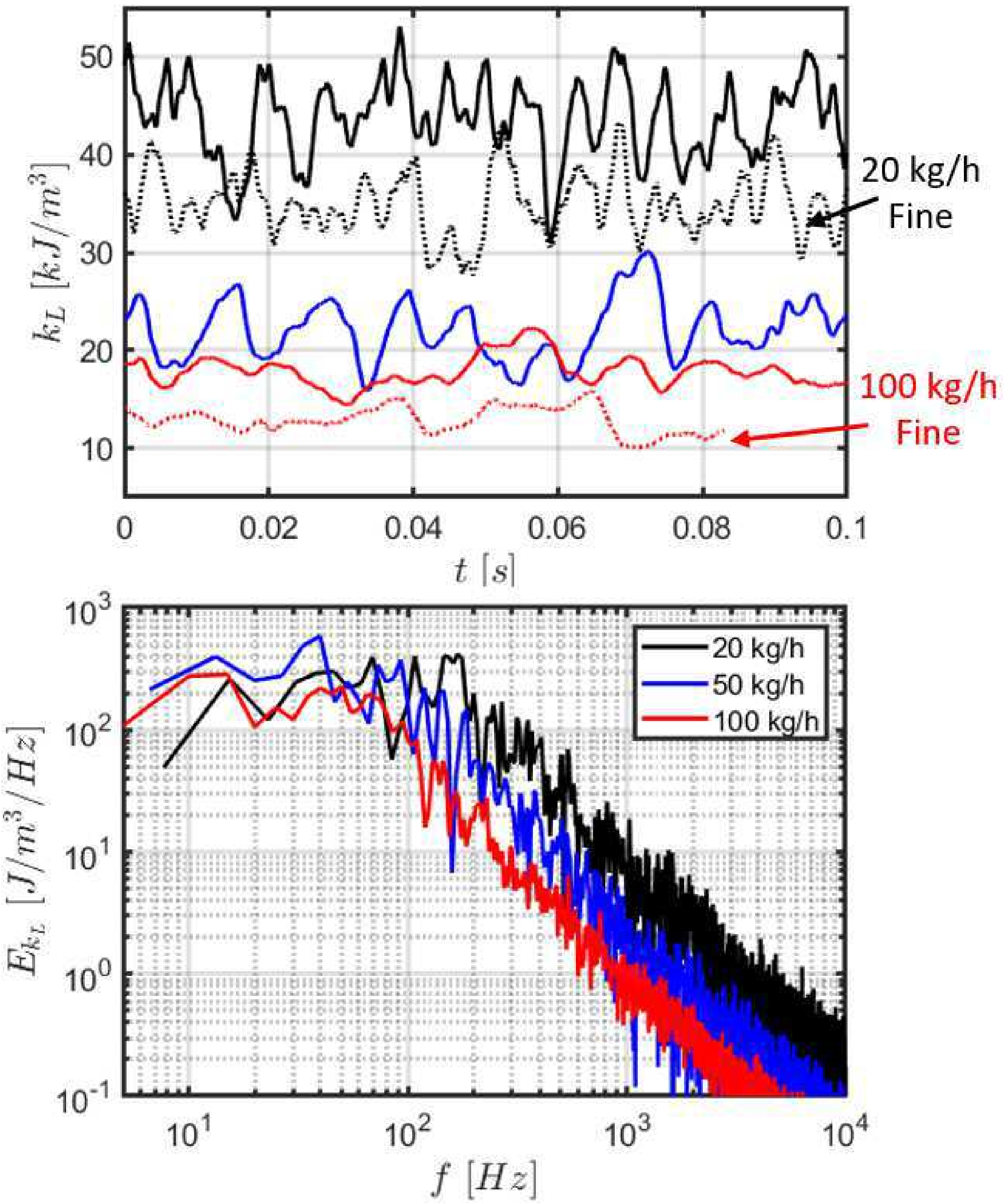
k_L $[kJ/m^3]$
50
40
30
20
10
0
0.02
0.04
0.06
0.08
0.1
t $[s]$
20 kg/h
Fine
100 kg/h
Fine
E_{k_L} $[J/m^3/Hz]$
10^3
10^2
10^1
10^0
10^{-1}
10^1
10^2
10^3
10^4
f $[Hz]$
20 kg/h
50 kg/h
100 kg/h

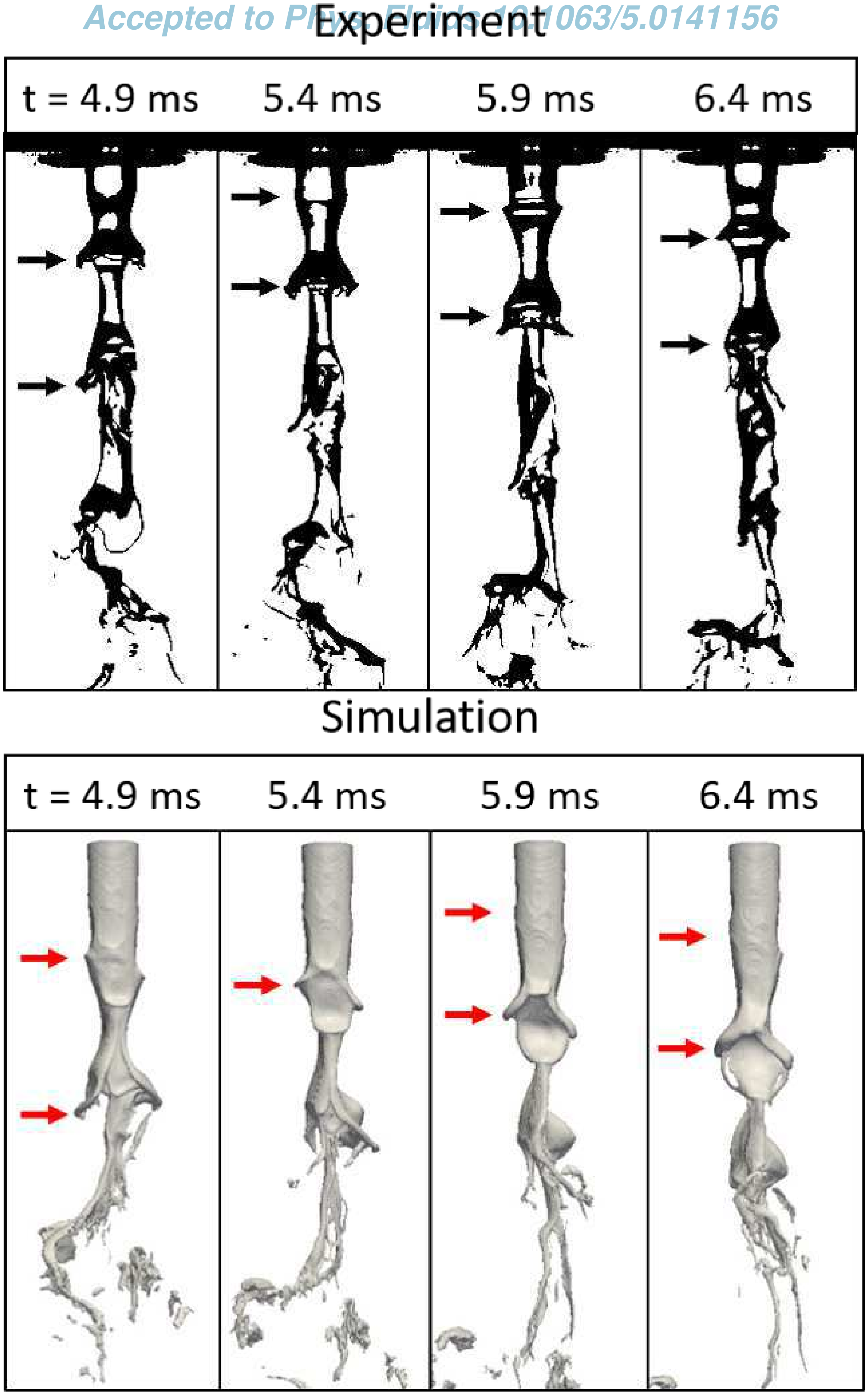
Experiment
t = 4.9 ms
5.4 ms
5.9 ms
6.4 ms
Simulation
t = 4.9 ms
5.4 ms
5.9 ms
6.4 ms

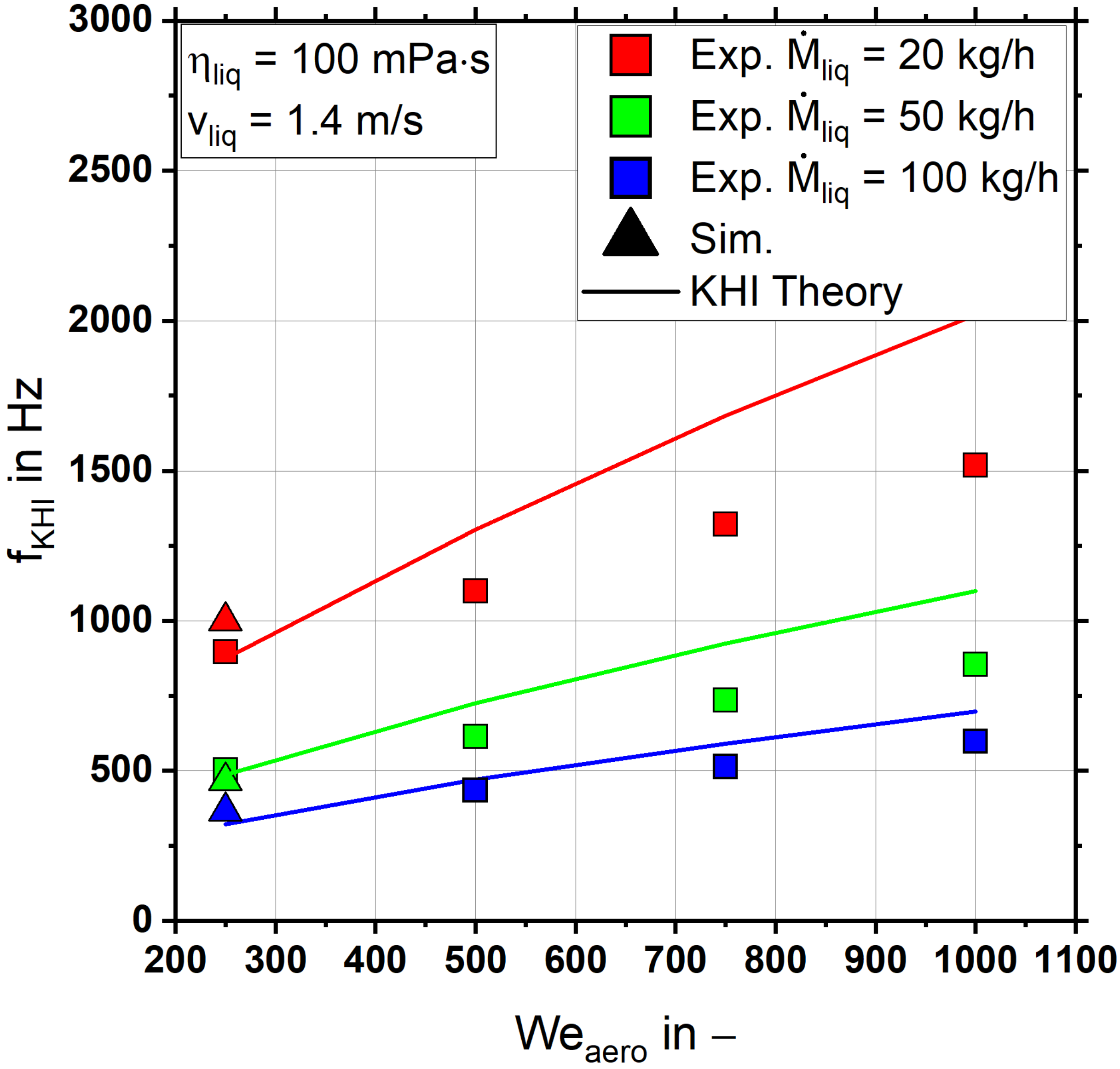PLEASE CITE THIS ARTICLE AS DOI: 10.1063/5.0141156